

Review

# Room Temperature Chemiresistive Gas Sensors Based on 2D MXenes

Ali Mirzaei <sup>1</sup>, Myoung Hoon Lee <sup>2</sup>, Haniyeh Safaeian <sup>1</sup>, Tae-Un Kim <sup>2</sup>, Jin-Young Kim <sup>3</sup>, Hyoun Woo Kim <sup>3,4,\*</sup> and Sang Sub Kim <sup>2,\*</sup>

<sup>1</sup> Department of Materials Science and Engineering, Shiraz University of Technology, Shiraz 71557-13876, Iran; mirzaei@sutech.ac.ir (A.M.); haniyeh.safaeyan@gmail.com (H.S.)

<sup>2</sup> Department of Materials Science and Engineering, Inha University, Incheon 22212, Republic of Korea; dm249@naver.com (M.H.L.); xodjs635@naver.com (T.-U.K.)

<sup>3</sup> The Research Institute of Industrial Science, Hanyang University, Seoul 04763, Republic of Korea; piadote@naver.com

<sup>4</sup> Division of Materials Science and Engineering, Hanyang University, Seoul 04763, Republic of Korea

\* Correspondence: hyounwoo@hanyang.ac.kr (H.W.K.); sangsub@inha.ac.kr (S.S.K.)

**Abstract:** Owing to their large surface area, two-dimensional (2D) semiconducting nanomaterials have been extensively studied for gas-sensing applications in recent years. In particular, the possibility of operating at room temperature (RT) is desirable for 2D gas sensors because it significantly reduces the power consumption of the sensing device. Furthermore, RT gas sensors are among the first choices for the development of flexible and wearable devices. In this review, we focus on the 2D MXenes used for the realization of RT gas sensors. Hence, pristine, doped, decorated, and composites of MXenes with other semiconductors for gas sensing are discussed. Two-dimensional MXene nanomaterials are discussed, with greater emphasis on the sensing mechanism. MXenes with the ability to work at RT have great potential for practical applications such as flexible and/or wearable gas sensors.

**Keywords:** 2D nanomaterials; MXene; sensing mechanism; gas sensor; RT



**Citation:** Mirzaei, A.; Lee, M.H.; Safaeian, H.; Kim, T.-U.; Kim, J.-Y.; Kim, H.W.; Kim, S.S. Room Temperature Chemiresistive Gas Sensors Based on 2D MXenes. *Sensors* **2023**, *23*, 8829. <https://doi.org/10.3390/s23218829>

Academic Editor: Victor Sysoev

Received: 27 September 2023

Revised: 17 October 2023

Accepted: 24 October 2023

Published: 30 October 2023



**Copyright:** © 2023 by the authors. Licensee MDPI, Basel, Switzerland. This article is an open access article distributed under the terms and conditions of the Creative Commons Attribution (CC BY) license (<https://creativecommons.org/licenses/by/4.0/>).

## 1. Introduction

Chemiresistive gas sensors, in which resistance is modulated in the presence of target gases, are fabricated mostly using metal oxide semiconductors (MOSs). This is not only owing to their high response, high stability, and fast dynamics, but also their low price and simple design [1,2]. Nevertheless, their working temperature is often high, up to 450 °C, leading to high power consumption. This is due to the fact that at low temperatures there is no sufficient energy for the gas molecules to overcome the adsorption barrier. However, with an increase in the sensing temperature, more gas molecules can be adsorbed on the surface of the sensor, leading to enhanced gas response. It should be noted that some metal oxides are able to work at RT [3]. However, some metal oxides have a very high resistance, in the range of Giga ohms, at RT, and some of them show too much noise and drift at RT, making difficult to measure their electrical properties. In contrast, MXenes have much lower resistance at RT with less noise, making them more favorable for sensing applications at RT. However, for some metal oxides which are able to work at RT, they generally can offer a higher response relative to MXene-based gas sensors due to their high intrinsic sensing properties.

Even though an increase of the sensing temperature is beneficial to have a higher response, it will result in significant power consumption. This is a disadvantage for gas sensors, especially for those working in remote areas, because of the limitation in power sources. Therefore, this issue limits the long-term use of high-temperature gas sensors in remote areas. Also, operation of the sensor at high temperatures for long times leads to a decrease in the sensor stability. Indeed, at high temperatures, more reactions occur on the

sensor surface, resulting in generation of new phases or even poisoning of the sensor, which eventually may degrade the sensing properties. Furthermore, at high temperatures ultrafine particles of the sensing layer may gradually sinter together, leading to agglomerations of particles and degradation of the sensing properties. Moreover, the detection of explosive gases, such as H<sub>2</sub> and CH<sub>4</sub>, at high temperatures is associated with an explosion risk. Hence, it is important to develop low- or room-temperature (RT) gas sensors [4].

In this regard, two-dimensional (2D) MXenes have gained more attention than other semiconductors for the realization of RT gas sensors because of their good conductivity, high surface area, ease of synthesis, tunable band gaps, ease of operation, and unique electrical characteristics. Furthermore, they have plenty of functional groups on their surfaces which are favorable sites for adsorption of gas molecules, which makes them very sensitive to changes in the gas concentrations in the surrounding atmosphere [5]. By controlling the type and amount of functional groups, it is possible to increase the sensitivity of these sensing materials. Owing to working at RT, they can be used for detection of explosive gases with high safety. In addition, they can be used in electronic devices and smartphones because of their low power consumption. Furthermore, they can be used for realization of flexible and wearable gas sensors which have applications in wearable electronic devices [6,7].

Previously, Li et al. [8] reviewed MXenes from chemical, electrochemical and energy-storage application points of view. Bhat et al. [9] discussed the stability of 2D MXenes for clean energy conversion and storage applications. Murali et al. [10] reviewed the synthesis of MXenes, their stability and photocatalytic applications. In another review paper, Murali and co-workers [11] discussed supercapacitor applications of MXenes. Also, recently, gas-sensing properties of MXenes have been reviewed. Ma et al. [7] reviewed flexible MXene-based gas sensors for wearable applications including gas sensors. Bhardwaj et al. reviewed MXene-based gas sensors [12]. Mehdi Aghaei and co-workers [13] discussed experimental and theoretical advances in MXene-based gas sensors. Zhang et al. [14] discussed strategies and challenges for improving performance of MXene-based gas sensors. Decaraj et al. discussed MXene and its nanocomposites for the detection of inorganic gases [15]. Xia et al. [16] discussed developments and challenges in MXene-based chemical gas sensors. Nahirniak and co-workers [17] reviewed MXene-heterojunctions for gas sensing application.

Riazi and co-workers [18] discussed MXene-based nanocomposites for gas sensing applications. Pei et al. [19] discussed gas sensing characteristics of Ti<sub>3</sub>C<sub>2</sub>T<sub>x</sub> MXene. Deshmukh et al. [20] Shina et al. [21] reviewed gas sensing and bio sensing properties of MXenes. Otgonbayar et al. discussed MXene sensors including gas sensors [22]. Ta et al. [23] discussed functional Ti<sub>3</sub>C<sub>2</sub>T<sub>x</sub> MXene for gas-sensing application. Jin et al. reviewed MXene-based textile sensors for wearable applications [24]. Radhakrishnan and co-workers [25] discussed MXenes for next-generation RT NO<sub>2</sub> gas sensors. Peng et al. [26] discussed Ti<sub>3</sub>C<sub>2</sub>T<sub>x</sub>-based gas sensors. Gautam et al. [27] discussed MXene and graphene for different applications, including gas-sensing application. Lee et al. [28] discussed MXene gas sensors from both theoretical and experimental points of view. Xin et al. [29] discussed MXenes in wearable sensing devices. Sivasankarapillai et al. [30] reviewed MXene-based materials for sensing applications. Simonenko et al. [31] discussed the gas-sensing properties of Ti<sub>2</sub>C<sub>2</sub>T<sub>x</sub> MXene. Tran et al. [32] reviewed modified MXenes for sensing studies. Li et al. reviewed gas-sensing properties of 2D MXenes [33].

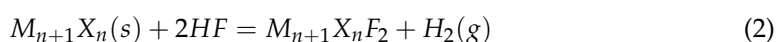
In this review, we have comprehensively reviewed the recent advancements in the development and application of RT chemiresistive gas sensors based on 2D MXenes, which have received less attention in previous review papers. In more detail, the objective of this review paper is to cover the synthesis methods, performance characteristics, sensing mechanism, and potential applications of these RT gas sensors. We start with an overview of 2D MXenes, explaining their general formula and structures. Then, we present a discussion of their synthesis methods. Following this, the gas-sensing properties of 2D MXenes in pristine, doped, decorated and composite forms are presented. Associated gas-sensing

mechanisms are also presented. Finally, we conclude with a summary of current challenges and future prospects. In this review paper, we only present the resistive MXene gas sensors at RT. However, it should be noted that MXenes also can be used for fabrication of other types of gas sensors. Also, there are some composites employing MXenes and working at higher temperatures. Herein, the focus was only on the resistive MXene-based gas sensors which are able to work at RT.

## 2. MXenes: A Brief Introduction

Since the discovery of 2D MXenes with nanosheet (NS) morphology by Gogotsi et al. [34] in 2011, MXenes have attracted much interest because of their features such as 2D morphology, high conductance, tunable bandgap, high mechanical flexibility, and hydrophilicity [35,36]. Their general formula is  $M_{n+1}X_nT_x$ , in which  $M$  represents the transition metal (Mo, Ti, Zr, Cr, etc.),  $X$  stands for “C” or “N” sites,  $n = 1$  to 4, and  $T_x$  ( $x$  is variable) indicates surface termination groups such as -H, -O, -OH, -F [37].

In these materials, layers of  $M$  atoms are arranged in a honeycomb-like 2D lattice intervened by  $X$  ions in the octahedral sites between adjacent metal layers. The precursors of MXenes are from MAX phases, with the formula  $M_{n+1}AX_n$  (MAX), where “ $n$ ” = 1 to 3,  $M$  is a transition metal, and  $A$  is a group 13–16 element. Figure 1a,b show the elements involved in MAX and the MXenes synthesized from the MAX phase, respectively [38]. Various routes are available for synthesizing MXenes [39,40]. However, they are generally produced by etching the MAX phase, in which the A-layer atoms are selectively etched to generate loosely stacked MX layers [41,42]. Mostly, the HF etchant with varying chemical composition is used to synthesis MXenes by the selective etching of Al atoms from Al-MAX phases. However, to achieve successful conversion of the MAX phase into the MXene, the control of the HF concentration, the reaction temperature and time are essential, since the M-Al bond strength depends on the type of  $M$  elements. It should be noted that intense etching lead to formation of defects, affecting the MXene quality. In addition, HF etching converts the MAX phase into accordion-like multilayered MXenes, in which individual NSs are held together by van der Waals forces and hydrogen bonds. During HF etching, the following reactions cause the removal of “A” atoms and generation of MXene.



Due to the high toxicity of HF, MXenes are also synthesized by using fluoride salt-derived in situ HF etching, fluoride-free etching, molten salt etching, and electrochemical-derived etching of MAX phases [43–45]. MXenes have also been used as templates for the synthesis of other materials [46]. Owing to their large surface area, controllable interlayer spacing, abundant functional groups, and unique electrical properties, MXenes are considered promising materials for realizing RT gas sensors [47,48]. Among MXenes, the most widely used for gas sensors is  $Ti_3C_2T_x$  MXene due to the following facts: (i) large specific area and numerous terminal functional groups (-OH, -O, and -F) on  $Ti_3C_2T_x$  MXene can lead to the strong interface chemical connection with semiconductors and form a Schottky junction. (ii) The high metallic conductivity of  $Ti_3C_2T_x$  assures rapid carrier migration. (iii) The exposed terminal metal sites on MXenes may result in more active reactivity than that of carbon materials [49].

One of the major limitations for the practical application of MXenes is their poor oxidation stability under ambient conditions. In fact, exposure to water, air, heat, and light degrades the 2D MXenes into a composite of metal oxide nanoparticles and amorphous carbon. The oxidation of the MXene NSs is generally initiated at surface defects/edges and then propagates to other parts of the nanosheet [43]. The oxidation and/or the state of MXene oxidation can be investigated by Raman spectroscopy [50]. For sensing applications, generally at RT there is no notable oxidation, as the sensing temperature is low. However, at high temperatures, MXene composition changes due to partial oxidation, which leads



RT [51]. Polymeric substrates are generally employed to realize flexible/wearable sensors owing to their low cost, flexibility, and stretchability. Flexible PI is widely used as a flexible substrate because of its excellent bendability, high thermal stability, and high chemical stability [52,53]. One fabricated sensor exhibited a response of 21% ( $(|R_g - R_a|)/R_a \times 100$ ) to 100 NH<sub>3</sub> at RT. The p-type semiconducting behavior of Ti<sub>3</sub>C<sub>2</sub>T<sub>x</sub> originated from the presence of H<sub>2</sub>O and oxygen on the surface of MXene, which were added during etching. NH<sub>3</sub> gas was adsorbed by both defects and functional groups, such as -O and -OH, on Ti<sub>3</sub>C<sub>2</sub>T<sub>x</sub> MXene. The bonding of NH<sub>3</sub> was stronger via hydrogen bonds, leading to the transfer of electrons from NH<sub>3</sub> to Ti<sub>3</sub>C<sub>2</sub>T<sub>x</sub>, which combined with the holes inside the Ti<sub>3</sub>C<sub>2</sub>T<sub>x</sub> sensor, leading to an increase in the resistance and generation of the sensing signal [51].

High-performance gas sensors should have low electrical noise, owing to their high conductivity, and strong signals owing to their strong and abundant adsorption sites [54]. However, it is difficult to satisfy these conditions. In fact, metal oxide gas sensors only show both a high signal and low noise at high temperatures due to the presence of activation energy. On the other hand, highly conductive channel materials are likely to yield low noise but lack the gas adsorption sites required for a high signal. In this regard, MXenes with both high conductivity and a high amount of adsorption sites are promising candidates. In an interesting study, Ti<sub>3</sub>C<sub>2</sub>T<sub>x</sub> MXenes were synthesized by etching using a mixture of lithium fluoride (LiF) and 9 M hydrochloric acid (HCl) while stirring. Then, they were delaminated by sonication. The Ti<sub>3</sub>C<sub>2</sub>T<sub>x</sub> sensor exhibited high selectivity to hydrogen-bonded gases over acidic gases and showed an empirical limit of detection (LOD) of 50 ppb. The Ti<sub>3</sub>C<sub>2</sub>T<sub>x</sub> sensor displayed significantly high signal-to-noise ratios (SNR) over the entire ppb range, and an SNR of 25.6 was obtained for acetone detection at 50 ppb. Both the metallic-like conductivity and presence of many adsorption sites are responsible for the high SNR of the sensor [54].

Because residual ions on the surface of Ti<sub>3</sub>C<sub>2</sub> during etching can affect the gas adsorption properties of MXene [55], it is necessary to explore the effect of the solution used for etching the MAX phase. Single-layer Ti<sub>3</sub>C<sub>2</sub> MXenes were prepared by etching the Ti<sub>3</sub>AlC<sub>2</sub> phase with a mixed solution of NaF/HCl. The sensor displayed a response of 6% ( $(|R_g - R_a|)/R_a \times 100$ ) to 500 ppm NH<sub>3</sub> gas at RT. Owing to the use of the NaF/HCl solution, the surface of Ti<sub>3</sub>C<sub>2</sub> was quite clean, as the Na ions were easily removed. This provided more adsorption sites for the NH<sub>3</sub> gas molecules. Density functional theory (DFT) calculations confirmed that the adsorption energy of NH<sub>3</sub> was higher than that of other gases; thus, it showed the strongest interaction with the sensing layer [56].

Because the -O and -OH intrinsic groups on the MXene surface act as favorable adsorption sites, their amounts can be increased to enhance the overall gas-sensing performance. In this context, plasma exposure is a highly promising technique with good control over parameters such as power, exposure duration, and atmosphere. In addition, the plasma exposure does not damage the structure of the MXenes. Exposure is particularly advantageous because the delicate MXene layers will not be damaged. In this context, a large number of oxygen functional groups were grafted onto delaminated Ti<sub>3</sub>C<sub>2</sub>T<sub>x</sub> MXenes via in situ plasma exposure. Air was first introduced at a flow rate of 400 sccm in a chamber at a vacuum level of 101 mbar. Next, the sensors were irradiated by plasma. The optimal sensor displayed a response of 13.8% ( $(|R_g - R_a|)/R_a \times 100$ ) to 10 ppm NO<sub>2</sub> at RT. DFT calculations revealed that the oxygen functional groups were associated with increased NO<sub>2</sub> adsorption energy, thereby enhancing the gas response [57].

The surface groups of the MXenes are responsible for their hydrophilic nature [58]. The introduction of hydrocarbon groups can reduce the hydrophilicity and enhance the sensing performance [59]. The modification was performed by substituting the -F groups with hydroxyls and subsequent treatment with trimethylacetic anhydride. Pristine Ti<sub>3</sub>C<sub>2</sub>T<sub>x</sub> exhibited a water contact angle (WCA) of 36.3°, reflecting its hydrophilic nature. After modification, the WCA increased to 78.5°, revealing the less hydrophilic nature of the treated MXene. In addition, the surface area of the treated sample was ~39 m<sup>2</sup> g<sup>-1</sup>, which

was remarkably higher than that of pristine  $\text{Ti}_3\text{C}_2\text{T}_x$  ( $\sim 10.35 \text{ m}^2 \text{ g}^{-1}$ ). The pristine and treated MXene sensors showed responses of 3 and 8% ( $[(R_g - R_a)/R_a] \times 100$ ) to 20 ppm ethanol at RT. Moreover, the response of the treated sensor to water vapor was reduced by 71% relative to pristine  $\text{Ti}_3\text{C}_2\text{T}_x$ , due to the less hydrophilic nature of the treated sensor. The treated  $\text{Ti}_3\text{C}_2\text{T}_x$  sensor was successfully used for alcohol detection via exhaled breath analysis [59].

Surface treatment is a feasible strategy to enhance the stability of MXene-based sensors at RT. 3-Aminopropyl triethoxysilane (APTES), as a silane coupling reagent, can not only decrease the oxidation of MXenes by the addition of a protective layer but can also add additional reactive groups such as  $-\text{NH}_2$  to MXene, which are promising for the detection of acidic gases. In this regard, delaminated  $\text{Nb}_2\text{CT}_x$  MXene was dispersed in a water and ethanol mixture of 1:9 ratio to provide enough water for a hydrolysis reaction. Subsequently, three different concentrations of APTES (0.1 mL, 0.2 mL, and 0.3 mL) were added to the above mixture. The hydrophilic  $-\text{NH}_2$  group with an electron-donating nature was useful for  $\text{NO}_2$  adsorption. The responses of 0.1, 0.2, and 0.3 mL APTES-functionalized  $\text{Nb}_2\text{CT}_x$  MXene sensors to 25 ppm  $\text{NO}_2$  gas were 22.5, 31.52, and 26.8% ( $[(R_g - R_a)/R_a] \times 100$ ), respectively, while that of the pristine sensor was only 12.5%. Hence, the addition of APTES to  $\text{Nb}_2\text{CT}_x$  MXenes enhanced the sensing response via amine functionalization. However, upon 0.3 mL addition of APTES, due to the increase in the number of Si-O-Si groups, the resistance of MXene increased, which limited the charge transfer and decreased the sensor response [60].

The positive response of MXenes to various gases can be attributed to the interlayer swelling. The resistance of the swollen 2D layers increases because of the limited out-of-plane flow of electrons. Therefore, preintercalation is a good method for optimizing the sensing features of MXenes. In this regard, the swelling of  $\text{Ti}_3\text{C}_2\text{T}_x$  MXenes treated with NaOH upon gas injection was explored using in situ XRD measurements.  $\text{Ti}_3\text{C}_2\text{T}_x$  MXene swelled upon ethanol injection, whereas no swelling was observed in a  $\text{CO}_2$  atmosphere. The swelling amount depends on the concentration of NaOH ions, and a 0.3 mM NaOH concentration resulted in the largest degree of swelling and the highest response to ethanol [61]. In another related study, first,  $\text{V}_2\text{CT}_x$  was synthesized by etching  $\text{V}_2\text{AlC}$  in a mixture of NaF and HCl. Secondly, the as-prepared  $\text{V}_2\text{CT}_x$  powder was further exfoliated by intercalation with dimethyl sulfoxide (DMSO). Finally, delaminated  $\text{V}_2\text{CT}_x$  powder was dispersed into a 10 mL NaOH solution (5 M) for 2 h. The alkalinized  $\text{V}_2\text{CT}_x$  sensor revealed an 80-times higher response to 50 ppm  $\text{NO}_2$  gas than the pristine sensor at RT. Because the alkalinized  $\text{V}_2\text{CT}_x$  sensor exhibited a positive gas response to both oxidizing and reducing gases, it was assumed that the sensing mechanism was related to interlayer swelling. The gas molecules diffuse into the layers of  $\text{V}_2\text{CT}_x$ , causing swelling of the layers. Furthermore, the high ratio of  $-\text{O}/-\text{F}$  surface terminal groups after alkalization is useful for gas sensing [62]. A similar alkalization process using a 5 M NaOH solution was reported for  $\text{Ti}_3\text{C}_2\text{T}_x$  with enhanced  $\text{NH}_3$  gas-sensing performance [63]. In another study,  $\text{V}_2\text{CT}_x$  MXene was deposited on a PI substrate and was able to detect 2 ppm hydrogen at RT. The amounts of oxygen and hydroxide surface groups on MXene were higher than  $-\text{F}$  groups; therefore, the sensor response was good because of the dominance of these surface groups. In addition, the presence of V ions as transition metals is beneficial for sensing  $\text{H}_2$  because of their catalytic activity towards  $\text{H}_2$  gas [64].

In another study related to  $\text{Mo}_2\text{CT}_x$ , first, 2 g of  $\text{Mo}_2\text{Ga}_2\text{C}$  powder was immersed in a  $\sim 25 \text{ wt}\%$  HF solution at  $55 \text{ }^\circ\text{C}$  for 8 days. The resultant  $\text{Mo}_2\text{CT}_x$  powder was dried in a vacuum oven. Then, 1 M TMAOH solution was used to delaminate the multilayer  $\text{Mo}_2\text{CT}_x$ . The delaminated  $\text{Mo}_2\text{CT}_x$  suspension was then collected after centrifugation. To study the effect of the  $\text{Mo}_2\text{CT}_x$  amount in the suspension on the sensing performance to toluene gas, five  $\text{Mo}_2\text{CT}_x$  suspensions (0.011, 0.033, 0.066, 0.36, and 0.66 mg/mL) were prepared. Also, the sonication times were varied between 0.5 to 8 h. For the sensors fabricated from the samples with the concentrations of  $\text{Mo}_2\text{CT}_x$  increased up to 0.066 mg/mL, many conducting paths were generated on the surface and the sensing area was increased so a

higher response was observed. Accordingly, the sensor prepared with a concentration of 0.066 mg/mL exhibited the highest sensing performance. With a further increase in the concentration, the deposited  $\text{Mo}_2\text{CT}_x$  sensor became thicker, and conducting paths were generated below the surface; hence, the modulation of the conductance was negligible. The optimal sonication time was determined to be 8 h. The sensing mechanism was attributed to the interaction between the benzene rings of the  $\text{C}_7\text{H}_8$  molecules and  $\text{MoC}_2\text{T}_x$ . Indeed, the benzene ring has a high activity and interacts more strongly with  $\text{MoC}_2\text{T}_x$ , resulting in a more significant change in the charge carriers inside the sensing layer. Furthermore, the  $-\text{CH}_3$  group in toluene further improved the activity of the benzene ring in the toluene molecules. In addition, according to DFT calculations, the adsorption energy of toluene on MXene was the highest, reflecting the intense interaction between toluene and the MXene surface, which contributed to the higher response to toluene [65].

The detection of methane at RT is difficult because of the high enthalpy of the C-H bonds and their nonpolar nature [66]. The  $\text{Ti}_2\text{CT}_x$  MXene sensor was used as a  $\text{CH}_4$  gas sensor at RT under visible light illumination. Under visible-light illumination, the sensing response to  $\text{CH}_4$  gas was significantly improved relative to that under dark conditions. The photocatalytic  $\text{CH}_4$  oxidation activity of  $\text{Ti}_2\text{CT}_x$  was responsible for its enhanced gas response. Under illumination, the generated electrons and holes generated highly active species ( $\text{O}^-$  or  $\text{OH}\bullet$  radical ions). In addition, the  $\text{Ti}^{4+}$  ions accepted the generated electrons and were converted to  $\text{Ti}^{3+}$  centers with high activity towards  $\text{CH}_4$  and the generation of  $\bullet\text{CH}_3$  active species. Then,  $\bullet\text{CH}_3$  reacted with  $\text{O}^-$  or  $\text{OH}\bullet$  species to produce final products. The released electrons increased the sensor resistance and contributed to the sensing signals [67].

### 2.1.2. Multilayered MXene Gas Sensors

Generally, van der Waals attractions between MXene NSs lead to self-stacking and agglomeration, which limits the adsorption sites on the sensor surface. Accordion-like  $\text{Ti}_3\text{C}_2\text{T}_x$  MXenes were synthesized using an HF etching method for acetone sensing. The response of the sensor to 100 ppm acetone was 100% ( $(|R_g - R_a|)/R_a \times 100$ ) at RT, and it was able to detect 250 ppb acetone with a fast response time ( $t_{\text{res}}$ ) of 53 s at RT. The high surface area is due to the accordion-like morphology of  $\text{Ti}_3\text{C}_2\text{T}_x$  as well as the presence of a large number of hydrogen bonds between the functional groups on the MXene surface and acetone vapor attributed to the sensing enhancement. However, the response of the gas sensor in the presence of 60% or higher RH was significantly decreased [68].

Mo-based MXenes, such as  $\text{Mo}_2\text{CT}_x$ , offer more conductance and higher reactivity than Ti-based MXenes; however, less attention has been paid to them. Three gas sensors based on multilayered  $\text{Mo}_2\text{CT}_x$  MXenes on glass, crystalline Si (cSi), and porous Si (pSi) substrates were used for  $\text{CO}_2$  sensing. The sensor deposited on glass Si substrate displayed the best response to  $\text{CO}_2$  gas, with a good response of 2.3% ( $(|R_g - R_a|)/R_a \times 100$ ) at RT to 50 ppm  $\text{CO}_2$  and fast  $t_{\text{res}}$  and recovery times ( $t_{\text{rec}}$ ) of 28 and 40 s, respectively [69]. However, at higher temperatures, the sensor deposited on pSi exhibited an enhanced response to  $\text{CO}_2$  gas. The enhanced gas response was justified by the lack of charge transfer from either the cSi or pSi substrates to MXene at RT. However, at higher temperatures, the charge transfer from these substrates to MXene leads to a decrease in resistance, which ultimately contributes to the sensing response.

Table 1 presents the RT gas-sensing properties of pristine MXene-based gas sensors. They are mostly used for detection of  $\text{NH}_3$ ,  $\text{NO}_2$ , ethanol, acetone and  $\text{CO}_2$  gases at RT.

**Table 1.** RT gas-sensing properties of pristine MXene-based gas sensors.

Sensing Material	Gas	Conc. (ppm)	Response (%) (( $ R_g - R_a $ )/ $R_a$ ) × 100)	Ref.
Pristine $Ti_3C_2T_x$	$NH_3$	100	21%	[51]
Pristine $Ti_3C_2T_x$	$NH_3$	500	6	[56]
Plasma-exposed $Ti_3C_2T_x$	$NO_2$	10	13.8	[57]
Surface-modified $Ti_3C_2T_x$	Ethanol	20	8	[59]
Surface-modified $Ti_3C_2T_x$	$NO_2$	25	26.8	[60]
Pristine $Ti_3C_2T_x$	Acetone	100	100	[68]
$Mo_2CT_x$	$CO_2$	50	2.3	[69]

It should be noted that the morphology of the sensing layer is mostly useful for enhancement of the response towards all gases and it has less effect on the selectivity. In general, MXene gas sensors in pristine form have good selectivity to  $NH_3$  gas. However, with modification with other materials, such as composite-making, doping or decoration, either selectivity to  $NH_3$  can be increased or selectivity towards another gas can be increased. Also, it should be noted that in general, the pristine MXene gas sensors suffer from incomplete recovery. However, with different modifications, the recovery rate can be increased to full recovery.

## 2.2. Composite MXene Gas Sensors

Generally, pristine MXene gas sensors suffer from low sensitivity and slow  $t_{rec}$ , limiting their applications. Composite fabrication is a solution to overcome these limitations. It is well known that composites enhance gas-sensing responses [70–73]. This is due to the high surface area of composites resulting from NS morphology and the formation of plenty of heterojunctions. The synthesis of MXene-based composites is reviewed in detail in [74]. In this section, we discuss the sensing performances of composite-based MXenes.

### 2.2.1. MXene–Metal Oxide Composites

The combination of MXenes with metal oxides is a promising strategy for enhancing the RT-sensing properties of the resultant composite, which generally leads to high-performance gas sensors at RT. Therefore, a  $SnO_2/Ti_3C_2T_x$  composite was synthesized hydrothermally. A mixture of MXene powder and stannic chloride pentahydrate ( $SnCl_4 \cdot 5H_2O$ ) was prepared. Then, it was put into a 50 mL Teflon-lined autoclave and heated at 180 °C for 12 h. The fabricated sensor offered a response of 40% ( $(|R_g - R_a|)/R_a$ ) × 100) to 40 ppm  $NH_3$  at RT, which was higher than a pristine sensor. In the composite, the 2D MXene provided a matrix with high conductivity, which enabled RT sensing.  $NH_3$  absorption at the defect sites on the MXene surface, as well as the interaction with functional groups, resulted in an enhanced gas response. Furthermore, the formation of heterojunctions between MXene and  $SnO_2$  NPs, which acted as resistance modulation sources, contributed to the sensing enhancement [75].

The influence of the amount of MXene in the  $Ti_3C_2T_x-SnO_2$  composite was also investigated.  $Ti_3C_2T_x$  MXene (10–40 wt%)- $SnO_2$  composites were prepared using a hydrothermal route for  $NO_2$  sensing at RT.  $SnO_2$  and  $Ti_3C_2T_x$  (10, 20, 30, and 40 wt%) were sonicated, and 0.32 g of urea was added into it along with the dropwise addition of 40- $\mu$ L HCl. The obtained solution was put inside an autoclave and heated at 120 °C for 8 h. All the  $SnO_2/MXene$  composite sensors exhibited superior performance to  $NO_2$  gas relative to pristine MXene. The composite sensor not only had a higher surface area (~25–30  $m^2/g$ ) than pristine MXene (8  $m^2/g$ ) due to combination of NS morphology of MXene with  $SnO_2$  NPs, but also a higher conductivity relative to pristine  $SnO_2$  NPs owing to the presence of MXene. The presence of MXene facilitated charge-carrier transport during gas sensing, resulting in faster  $t_{res}$  and  $t_{rec}$ . In addition, the functional groups of the  $Ti_3C_2T_x$  MXenes are favorable sites for gas adsorption. The sensor with the lowest amount of MXene (10 wt%) showed some agglomeration between the  $SnO_2$  NPs, while the sensor with 20 wt%  $Ti_3C_2T_x$

showed the maximum performance. The response decreased with a further increase in the MXene amount, which was related to the presence of enormous -OH termination groups, hindering the number of active sites for NO<sub>2</sub> gas. For the optimal gas sensor, because of the sufficient number of gas adsorption active sites and enough charge-carrier transportation as a result of fewer agglomerated SnO<sub>2</sub> NPs, a high response was observed. The formation of heterojunctions between MXene and SnO<sub>2</sub> and subsequent modulation of the barrier height in the presence of NO<sub>2</sub> gas also contributed to the sensing signal (Figure 2). SnO<sub>2</sub> and MXene have different work functions; hence, upon intimate contact, electrons from MXene move to SnO<sub>2</sub> to equate the Fermi levels inside of the contacts. This leads to the formation of potential barriers to the flow of electrons in interfaces in air. Upon subsequent exposure to NO<sub>2</sub> gas, more electrons are abstracted from the sensing layer, and this increases the height of the potential barrier. Accordingly, the resistance will be significantly increased [76].

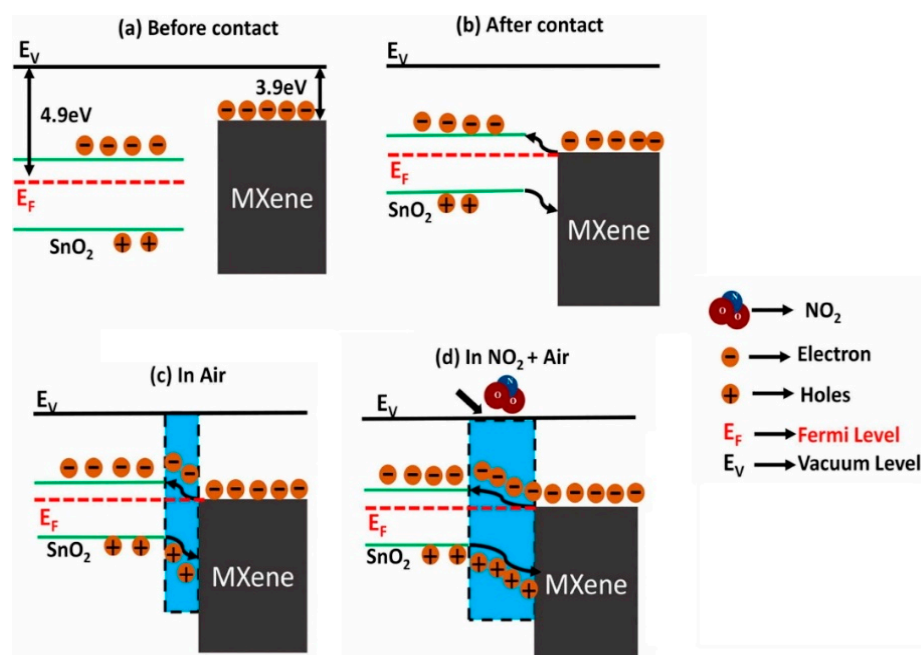


**Figure 2.** Energy band levels of MXene/SnO<sub>2</sub> (a) before and after contact in (b) vacuum (c) air (d) NO<sub>2</sub> gas [76]. With permission from Elsevier.

In another study, Ti<sub>3</sub>C<sub>2</sub>T<sub>x</sub> MXene/SnO NSs were prepared via a hydrothermal route. After magnetic stirring of the Ti<sub>3</sub>C<sub>2</sub>T<sub>x</sub> MXene solution for 1 h, SnCl<sub>2</sub>·2H<sub>2</sub>O and urea were added into the above solution, and then 30 μL HCl (36–38%) was added dropwise. Then, it was hydrothermally treated at 120 °C for 24 h in a Teflon autoclave. The responses of the fabricated sensor to 200 ppm NH<sub>3</sub> was 7.8 at RT.  $t_{res}$  and  $t_{rec}$  were 1 and 2 min, respectively. Figure 3a shows the sensing mechanism of the sensor. Heterojunctions were formed between the n-type SnO NSs and p-type Ti<sub>3</sub>C<sub>2</sub>T<sub>x</sub> in air due to differences between the work functions. Accordingly, potential barriers were formed in interfaces between these two materials in air. Subsequent modulation of the heights of these barriers in an NH<sub>3</sub> atmosphere resulted in the resistance change (Figure 3b). In addition, the high surface area originating from the 2D nature of both sensing materials and the existence of surface groups resulted in a high sensor response [77].

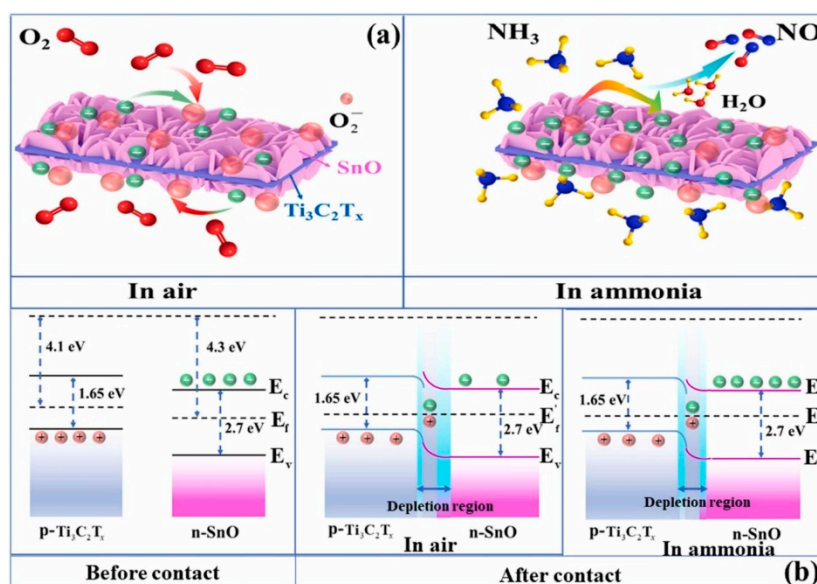


**Figure 3.** (a) Schematic of  $\text{NH}_3$ -sensing mechanism and (b) the energy bands of  $\text{Ti}_3\text{C}_2\text{T}_x$  MXene and SnO before contact, and after contact in air and  $\text{NH}_3$  [77]. With permission from Elsevier.

$\text{SnO}_2$  NPs (5–10 nm) were dispersed on the  $\text{Ti}_3\text{C}_2\text{T}_x$  MXene surface during the hydrothermal synthesis.  $\text{SnCl}_4 \cdot 5 \text{H}_2\text{O}$  and different volumes (10, 15, 20 and 25 mL) of the few-layered  $\text{Ti}_3\text{C}_2\text{T}_x$  colloidal solution were poured to form a homogeneous mixture by means of electrostatic self-assembly; the obtained samples were named as 4.8%, 9.2%, 13.1% and 16.8%  $\text{Ti}_3\text{C}_2\text{T}_x$ - $\text{SnO}_2$  composites, respectively. Then,  $\text{CO}(\text{NH}_2)_2$  dissolved in various deionized water (30, 25, 20 and 15 mL) was dripped slowly into the mixture and stirred for 0.5 h. The resulting mixed solution was subsequently transferred into a 100 mL Teflon-lined autoclave and kept at 180 °C for 12 h.

A small amount of  $\text{TiO}_2$  was formed during synthesis. A high response of 25% ( $(|R_g - R_a|)/R_a \times 100$ ) to 100 ppm  $\text{NH}_3$  gas was recorded at RT for the optimal sensor with 13.1% MXene. The  $\text{SnO}_2$  NPs formed a loose porous structure and provided a large surface area and abundant active sites for sensing reactions. In addition,  $\text{TiO}_2$  NPs formed along the MXene interlayers, preventing their restacking. The formation of heterojunctions between  $\text{Ti}_3\text{C}_2\text{T}_x$  MXene,  $\text{TiO}_2$ , and  $\text{SnO}_2$  NPs led to resistance modulation during the injection of  $\text{NH}_3$  gas (Figure 4) [78].

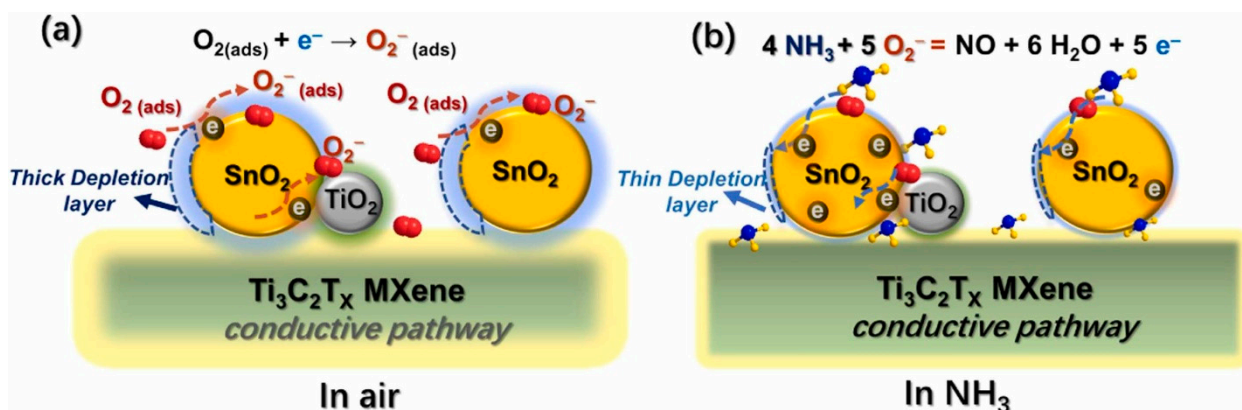


**Figure 4.**  $\text{NH}_3$ -sensing mechanism of the  $\text{Ti}_3\text{C}_2\text{T}_x$ - $\text{SnO}_2$  composite in (a) air and (b)  $\text{NH}_3$  [78]. With permission from Elsevier.

An ultrasonic method was used to prepare  $\text{NiO}/\text{Ti}_3\text{C}_2\text{T}_x$  MXene nanocomposites.  $\text{NiO}$  and MXene powders were dissolved in deionized water and then subjected to ul-

trasonic treatment for 5 h. Then, it was centrifuged to separate the precipitate, and the NiO/Ti<sub>3</sub>C<sub>2</sub>T<sub>x</sub> MXene composite was obtained. The sensor exhibited a high response of 6.13% ( $(|R_g - R_a|)/R_a \times 100$ ) to 50 ppm NH<sub>3</sub> at RT, which was ~9 times more than that of the pristine MXene sensor. Well-dispersed NiO particles in the interlayers of the accordion-like MXene not only prevented agglomeration but also increased the surface area (Figure 5a). Hence, it improves the absorption and diffusion of NH<sub>3</sub> molecules. Furthermore, many functional groups on MXene can easily form strong hydrogen bonds with NH<sub>3</sub> gas. In addition, the high conductivity of MXenes accelerates charge transfer, thereby enhancing the gas response. The formation of heterojunctions also accounted for the sensing enhancement. Figure 5b shows the modulation of the energy bands of the NiO/Ti<sub>3</sub>C<sub>2</sub>T<sub>x</sub> MXene nanocomposite sensor in air and in NH<sub>3</sub> gas [79].

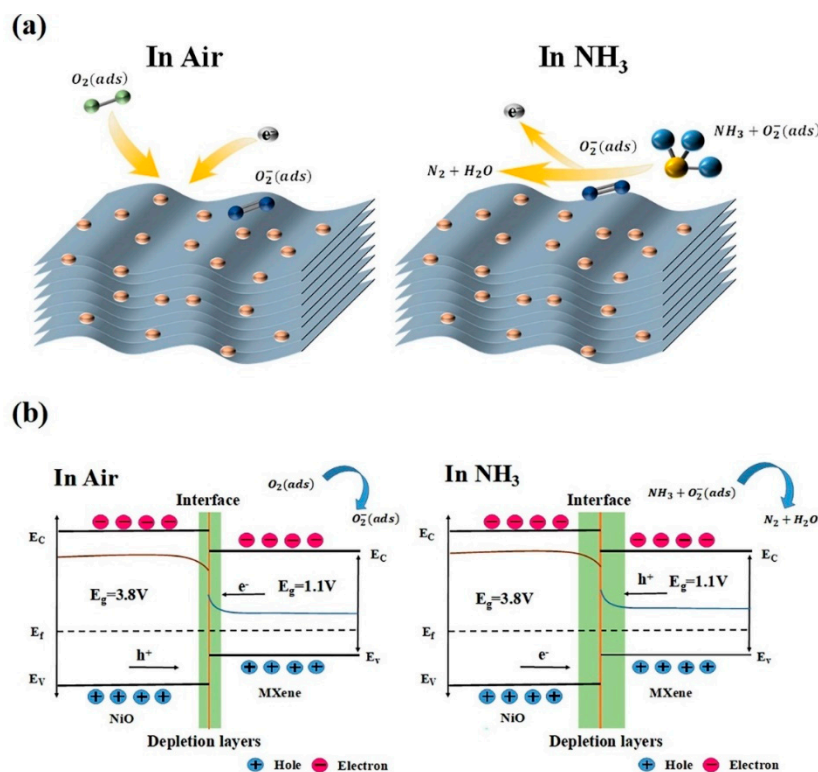


**Figure 5.** (a) Schematic image of the mechanism of NiO/Ti<sub>3</sub>C<sub>2</sub>T<sub>x</sub> MXene sensor. (b) Formation of heterojunctions between NiO and MXene in air and acetone [79]. With permission from Elsevier.

A MXene/NiO composite was synthesized via an in situ precipitation method. A NiSO<sub>4</sub>·6H<sub>2</sub>O and MXene solution was prepared, and then a NaOH aqueous solution was dropped into the solution. After being stirred for 2 h, the precipitates were collected and washed three times with deionized water and three times with ethanol. Then, the samples were dried at 60 °C for 24 h. Finally, the MXene/NiO composite materials were obtained after being calcined at 350 °C for 2 h under N<sub>2</sub> atmosphere. The sensor response to 50 ppm HCHO gas was 8.8 at RT. Based on FTIR analysis, numerous hydroxyl and other oxygen-containing functional groups were present on the sensor surface, which are important for NH<sub>3</sub> gas sensing. Also, based on the in situ FTIR analysis (Figure 6), by increasing exposure time of HCHO gas, the peaks at 1352 and 1413 cm<sup>-1</sup> were attributed to molecularly adsorbed HCHO on the sensing material. The peaks at 1340 and 1557 cm<sup>-1</sup> were related to the COO<sup>-</sup> symmetric stretching and asymmetric stretching vibrations of formate species, respectively. The peak at 1510 cm<sup>-1</sup> was related to the vibrations of formate species. Hence, formate species are intermediate products of HCHO adsorption [80].

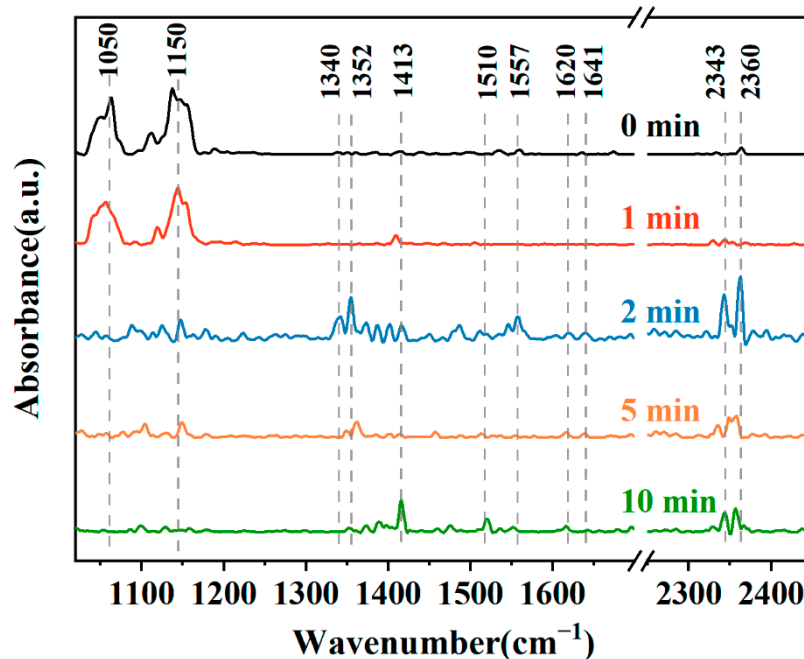
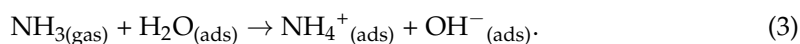
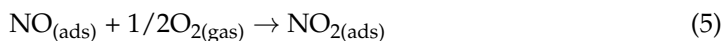
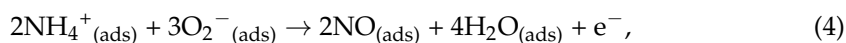


Figure 6. In situ FTIR spectra of the MXene/NiO sensor exposed to HCHO gas [80].

$\text{Ti}_3\text{C}_2\text{T}_x$  MXene (30–100 wt%)/ $\text{In}_2\text{O}_3$  composite gas sensors were prepared for  $\text{NH}_3$  sensing studies. Initially,  $\text{In}_2\text{O}_3$  was prepared by dissolving  $\text{In}(\text{NO}_3)_3 \cdot x\text{H}_2\text{O}$  in a mixed solution of ethanol and 25 wt%  $\text{NH}_3 \cdot \text{H}_2\text{O}$  and subsequent hydrothermal synthesis at  $100^\circ\text{C}$  for 24 h. Then,  $\text{In}_2\text{O}_3/\text{MXene}$  with different amounts of MXene was sonicated, and after vacuum drying at  $60^\circ\text{C}$  for 6 h the composites were prepared. The sensor with 40 wt% MXene exhibited a high response of 100% ( $[(1 R_g - R_a) / R_a] \times 100$ ) to 20 ppm  $\text{NH}_3$  gas, which was 30 times more than the response of pristine MXene. Moreover, the response to  $\text{NH}_3$  increases with increasing RH in the gas mixture. In a humid environment, the ammonia molecules were “solvated” and the released electrons in a humid environment increased the sensor resistance:



Then,  $\text{NH}_4^+$  reacted with  $\text{O}_2^-(\text{ads})$  as follows:



The generation of gaseous nitric oxides was confirmed by in situ diffuse reflectance infrared Fourier transform (DRIFT) spectroscopy during the sensing process. The generated electrons combine with holes on MXene, resulting in an increase in resistance and an enhanced response [81]. In another study dealing with MXene/ $\text{SnS}_2$  heterojunction sensors [82], similar to [81], the response increased under humid conditions. In situ DRIFT analysis confirmed the production of nitric oxides during the  $\text{NH}_3$  reaction on the sensor surface in a humid environment. In addition, the enhanced response to  $\text{NH}_3$  gas was attributed to the formation of heterojunctions between MXene and  $\text{SnS}_2$ . DFT calculations demonstrated strong  $\text{NH}_3$  adsorption on the sensor surface.

$\text{In}_2\text{O}_3$  nanocubes/ $\text{Ti}_3\text{C}_2\text{T}_x$  MXene composites were prepared using a hydrothermal method.  $\text{In}_2\text{O}_3$  nanocubes were dissolved in ethanol via ultrasonication, and then APTES was poured dropwise into the above solution to make the surface positively charged. Next,  $\text{Ti}_3\text{C}_2\text{T}_x$  MXene solution was slowly added to the above solution, and then it was put into a Teflon-lined autoclave. After the hydrothermal reaction at  $120^\circ\text{C}$  for 14 h,

the  $\text{In}_2\text{O}_3/\text{Ti}_3\text{C}_2\text{T}_x$  MXene composites were obtained. The  $\text{In}_2\text{O}_3$  nanocubes were well dispersed between the  $\text{Ti}_3\text{C}_2\text{T}_x$  MXene NSs layers (Figure 7a). The sensor exhibited a high response of 29.6% ( $[(|R_g - R_a|)/R_a] \times 100$ ) to 5 ppm methanol gas at RT. In addition,  $t_{\text{res}}$  and  $t_{\text{rec}}$  were very fast (6.5/3.5 s). The sensing materials had a mesoporous structure; thus, the target gas easily diffused into the deeper parts of the sensor. The existence of many functional groups on MXene which acted as active sites for the adsorption of methanol, as well as the generation of Schottky junctions between  $\text{Ti}_3\text{C}_2\text{T}_x$  MXene and the  $\text{In}_2\text{O}_3$  nanocubes, accounted for the sensing improvement (Figure 7b) [83]. Due to the difference between the work functions of  $\text{Ti}_3\text{C}_2\text{T}_x$  and  $\text{In}_2\text{O}_3$  materials, electrons move from  $\text{Ti}_3\text{C}_2\text{T}_x$  to  $\text{In}_2\text{O}_3$ , resulting in band bending and formation of potential barriers in interfaces. In a methanol atmosphere, the height of these barriers changes due to the return of electrons to a sensing layer, leading to modulation of the electrical resistance.

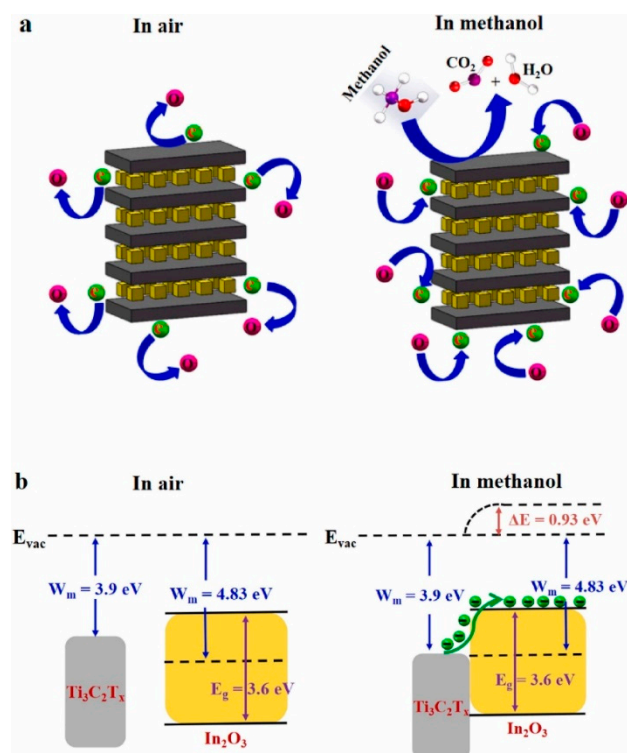


**Figure 7.** (a) Schematic of the sensing mechanism and (b) the energy band diagram of  $\text{In}_2\text{O}_3/\text{Ti}_3\text{C}_2\text{T}_x$  MXene composites in air and methanol [83]. With permission from Elsevier.

In other interesting research, the MOF-derived hollow  $\text{In}_2\text{O}_3$  microbubbles (2–5  $\mu\text{m}$ ) were attached on the exfoliated  $\text{Ti}_3\text{C}_2\text{T}_x$  MXene. Initially, Indium nitrate hydrate and 1,4-benzenedicarboxylic acid ( $\text{H}_2\text{BDC}$ ) were dissolved in *N,N*-dimethylformamide (DMF) under mechanical stirring to form a homogeneous solution at RT. Next,  $\text{Ti}_3\text{C}_2\text{T}_x$  MXene solution (0.1 g/mL) was added to the above solution. Subsequently, it was transferred into the oil bath and the temperature was maintained at 120  $^\circ\text{C}$  for 30 min. To obtain the final MOF-derived  $\text{In}_2\text{O}_3/\text{Ti}_3\text{C}_2\text{T}_x$  MXene composite material, it was annealed at 500  $^\circ\text{C}$  for 3 h to remove the organic template. The sensor displayed a response of 60.6% ( $[(|R_g - R_a|)/R_a] \times 100$ ) to 5 ppm  $\text{NH}_3$  gas at RT, along with a fast  $t_{\text{res}}/t_{\text{rec}}$  of 3/2 s and outstanding selectivity. Figure 8a shows the possible sensing mechanism for  $\text{NH}_3$  gas. The work function of MIL- $\text{In}_2\text{O}_3$  is 4.28 eV and that of  $\text{Ti}_3\text{C}_2\text{T}_x$  is 4.79 eV. Hence, upon contact, electrons move from MIL- $\text{In}_2\text{O}_3$  to  $\text{Ti}_3\text{C}_2\text{T}_x$  to equate the Fermi levels. This results in band bending and the formation of potential barriers in interfaces. In a  $\text{NH}_3$  atmosphere, the electrons come back to the surface of the sensor, resulting in changes of potential barriers and changes in the flow of electrons. Accordingly, the resistance is modulated, which contributes to the sensing signal (Figure 8b,c). Hence, the formation of

p-n heterojunctions, good intrinsic sensing properties of  $\text{In}_2\text{O}_3$ , high surface area provided by MXene, presence of numerous surface groups on MXene, and high mobility of carriers in MXene all contributed to the sensing enhancement. Based on the DFT calculations, the adsorption energies of  $\text{NH}_3$  molecules on the optimized configurations of  $\text{In}_2\text{O}_3$  and  $\text{Ti}_3\text{C}_2\text{T}_x$  MXene (Figure 8d,e) were  $-8.1$  and  $-3.7$  eV, respectively, reflecting the fact that  $\text{In}_2\text{O}_3$  was the main source of the resistance change in the gas sensor [84].

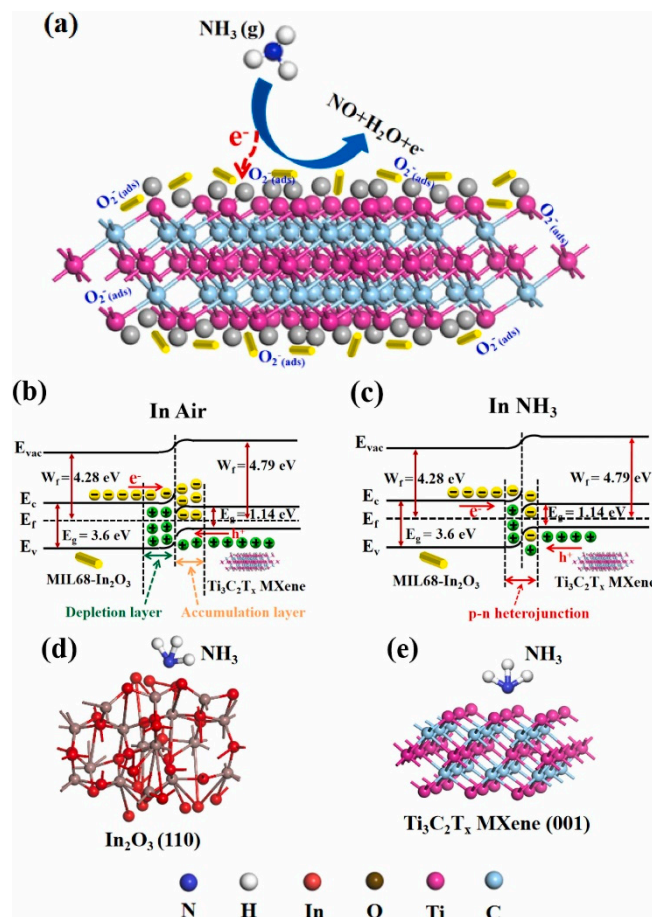


**Figure 8.** (a) Schematic of the mechanism of MOF-derived  $\text{In}_2\text{O}_3/\text{Ti}_3\text{C}_2\text{T}_x$  MXene composites to  $\text{NH}_3$  (b,c) corresponding the energy bands in air and  $\text{NH}_3$  gas. (d,e) Optimized configurations of  $\text{NH}_3$  adsorption on  $\text{In}_2\text{O}_3$  and  $\text{Ti}_3\text{C}_2\text{T}_x$  MXene [84]. With permission from Elsevier.

$\alpha\text{-Fe}_2\text{O}_3/\text{Ti}_3\text{C}_2\text{T}_x$  MXene composite with a high surface area of  $47.8$  m<sup>2</sup>/g was hydrothermally synthesized at  $120$  °C/14 h using  $\alpha\text{-Fe}_2\text{O}_3$  nanocubes and  $\text{Ti}_3\text{C}_2\text{T}_x$  MXene. The response to 5 ppm acetone was 16.6% ( $(|R_g - R_a|)/R_a \times 100$ ), along with very fast  $t_{\text{res}}$  and  $t_{\text{rec}}$  (5/5 s) at RT, which were better than those of pristine sensors. Apart from the formation of heterojunctions between  $\text{Fe}_2\text{O}_3$  and MXene, the flake-like morphology decreased the agglomeration of  $\alpha\text{-Fe}_2\text{O}_3$  and promoted the adsorption of gas molecules due to the higher surface area. In addition, the presence of defects and functional groups on  $\text{Ti}_3\text{C}_2\text{T}_x$  MXene facilitated the interaction between acetone and the gas sensor. Based on DFT calculations, the band gaps of  $\text{Fe}_2\text{O}_3$  and MXene were determined to be 2.2 and 0 eV, respectively, reflecting the high metallic conductivity of MXene. Hence,  $\text{Ti}_3\text{C}_2\text{T}_x$  MXene with high conductivity was able to easily accept electrons, resulting in a significant resistance change of the  $\alpha\text{-Fe}_2\text{O}_3/\text{Ti}_3\text{C}_2\text{T}_x$  MXene composite. Furthermore, the adsorption energy of acetone on  $\alpha\text{-Fe}_2\text{O}_3/\text{Ti}_3\text{C}_2\text{T}_x$  MXene heterojunction was  $-6.7$  eV, which was higher than that on pristine  $\alpha\text{-Fe}_2\text{O}_3$  ( $-0.2$  eV) and  $\text{Ti}_3\text{C}_2\text{T}_x$  ( $-5.9$  eV) sensors [85].

A rose-like  $\alpha\text{-Fe}_2\text{O}_3/\text{Ti}_3\text{C}_2\text{T}_x$  MXene composite was prepared using hydrothermal synthesis at  $120$  °C/14 h for  $\text{NH}_3$  sensing. The surface areas of composite, pristine  $\alpha\text{-Fe}_2\text{O}_3$

$\text{Fe}_2\text{O}_3$ , and  $\text{Ti}_3\text{C}_2\text{T}_x$  MXene were 29.2, 9.3, and  $1.4\text{ m}^2/\text{g}$ , respectively. The enhanced surface area was related to the special morphology of the composite. The composite sensor offered a response of 18.3% ( $[(|R_g - R_a|)/R_a] \times 100$ ) and fast  $t_{\text{res}}$  and  $t_{\text{rec}}$  of  $<2.5\text{ s}$  to 5 ppm  $\text{NH}_3$  gas at RT. The good response of the sensor was attributed to high surface area, the presence of abundant functional groups, as well as the formation of  $\alpha\text{-Fe}_2\text{O}_3/\text{Ti}_3\text{C}_2\text{T}_x$  MXene heterojunctions in air and subsequent modulation in a  $\text{NH}_3$  gas atmosphere (Figure 9). The work function of  $\alpha\text{-Fe}_2\text{O}_3$  is 5.9 eV and that of  $\text{Ti}_3\text{C}_2\text{T}_x$  is 4.79 eV. Accordingly, when they are in contact, electrons from  $\text{Ti}_3\text{C}_2\text{T}_x$  flow to  $\alpha\text{-Fe}_2\text{O}_3$ , while the holes move in different directions to equate the Fermi levels. This results in the formation of heterojunctions with band bending and the generation of potential barriers. Accordingly, the flow of electrons becomes difficult in air. In a  $\text{NH}_3$  atmosphere and upon the release of electrons, the heights of these potential barriers change and this eventually leads to a change of the resistance. In addition, based on the Knudsen diffusion theory,  $\text{NH}_3$  gas, with a lighter mass relative to the other tested gases, showed a fast diffusion rate, which resulted in the selectivity of the sensor to this gas [86].

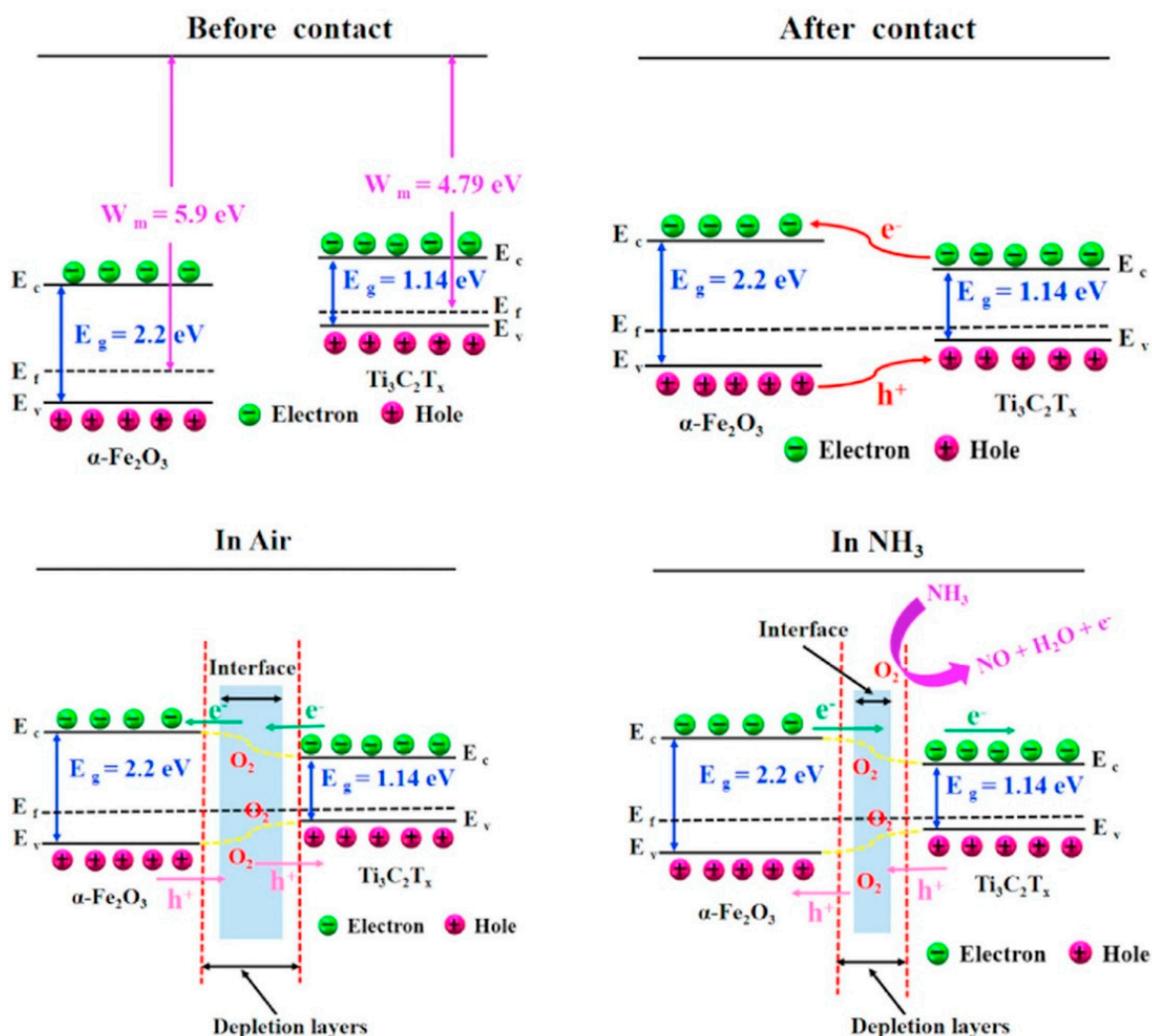


**Figure 9.** Energy bands of MXene and  $\text{Fe}_2\text{O}_3$  before and after contact in the present of air and  $\text{NH}_3$  [86]. With permission from Elsevier.

However, MXene-based sensors that can detect ppb levels in gases have rarely been reported. In this context, a  $\text{Ti}_3\text{C}_2\text{T}_x/\text{WO}_3$  nanocomposite with a large surface area of  $36\text{ m}^2/\text{g}$  was synthesized hydrothermally at  $180\text{ }^\circ\text{C}/24\text{ h}$ . It displayed a high response of 78% ( $[(|R_g - R_a|)/R_a] \times 100$ ) to 200 ppb  $\text{NO}_2$  at RT, which was higher than the bare

WO<sub>3</sub> sensor (9.8%) with short  $t_{res}$  (3 min) and  $t_{rec}$  (75 s). In addition to the modulation of the resistance in the interface areas between MXene and WO<sub>3</sub> due to the formation of heterojunctions, the high surface area and porous structure of the composite accounted for the sensing enhancement. Furthermore, the highly conductive nature of the MXene phase facilitates charge flow and diffusion of gas inside the sensor [87].

WO<sub>3</sub> NPs attached to Ti<sub>3</sub>C<sub>2</sub>T<sub>x</sub> NSs were synthesized using ultrasonication for 3 h at a frequency of 22 kHz and power of 150 W. The sensor with 50 wt% WO<sub>3</sub> exhibited a high response of 22.3% ( $(|R_g - R_a|)/R_a \times 100$ ) to 1 ppm NH<sub>3</sub> at RT, which was more than 15 times higher than the pristine Ti<sub>3</sub>C<sub>2</sub>T<sub>x</sub> sensor. The porous structure with a specific surface area of 6.129 m<sup>2</sup>/g was beneficial for the diffusion of gas molecules and enhanced response. In addition, the defects in WO<sub>3</sub> provide additional sites for the adsorption of NH<sub>3</sub> molecules on the composite surface. In addition, the functional groups on MXene act as adsorption sites for NH<sub>3</sub> gas molecules. Finally, the formation of p-n heterojunctions is attributed to the sensing mechanism [88].

A Ti<sub>3</sub>C<sub>2</sub>T<sub>x</sub> MXene/CuO composite was synthesized using a solvothermal method at 120 °C/14 h for RT NH<sub>3</sub> sensing. The sensor exhibited a high response of 46.7% ( $(|R_g - R_a|)/R_a \times 100$ ) to 5 ppm NH<sub>3</sub> with fast  $t_{res}$  (12 s) and  $t_{rec}$  (25 s). The surface area of the composite was 30.94 m<sup>2</sup>/g, which was higher than that of pristine CuO (~25.55 m<sup>2</sup>/g) and Ti<sub>3</sub>C<sub>2</sub>T<sub>x</sub> MXene (~2.75 m<sup>2</sup>/g). This resulted in more adsorption sites for incoming NH<sub>3</sub> gas molecules. In addition, the formation of p-p heterojunctions between the two components and the presence of surface functional groups on MXene, which formed strong hydrogen bonds with NH<sub>3</sub> gas, contributed to resistance modulation. Based on density functional theory (DFT) calculations, the adsorption energy of NH<sub>3</sub> on CuO was larger than that on Ti<sub>3</sub>C<sub>2</sub>T<sub>x</sub> MXene, confirming that gas sensing was mostly governed by CuO [89]. Ti<sub>3</sub>C<sub>2</sub>T<sub>x</sub>/CuO nanocomposites with a mesoporous nature and high surface area (26.9 m<sup>2</sup>/g) were prepared using a hydrothermal approach at 150 °C/12 h. The sensor exhibited a response of 57% ( $(|R_g - R_a|)/R_a \times 100$ ) to 50 ppm NO<sub>2</sub> at RT. The enhanced gas-sensing performance is related to the formation of CuO-Ti<sub>3</sub>C<sub>2</sub>T<sub>x</sub> heterojunctions and the presence of more oxygen vacancies relative to pristine Ti<sub>3</sub>C<sub>2</sub>T<sub>x</sub> [90].

Accordion-like V<sub>2</sub>CT<sub>x</sub> MXene was synthesized by the selective etching of V<sub>2</sub>AlC, and V<sub>2</sub>CT<sub>x</sub>/V<sub>3</sub>O<sub>7</sub> nanocomposites were prepared by the partial conversion of V<sub>2</sub>CT<sub>x</sub> to V<sub>3</sub>O<sub>7</sub> due to oxidation at different temperatures (50–250 °C). The V<sub>2</sub>CT<sub>x</sub>/V<sub>3</sub>O<sub>7</sub> nanocomposite obtained at 250 °C was used for sensing studies. The sensor exhibited a response of 16% ( $(|R_g - R_a|)/R_a \times 100$ ) to 100 ppm NO<sub>2</sub> at RT. The partial oxidation of V<sub>2</sub>CT<sub>x</sub> led not only to an increase in the response of the V<sub>2</sub>CT<sub>x</sub>/V<sub>3</sub>O<sub>7</sub> material but also to some change in its selectivity. In fact, the pristine sensor exhibited the highest response to NH<sub>3</sub> gas, while the composite showed the highest response to NO<sub>2</sub> gas at RT. The increase in the response of the nanocomposite sensor was related to the formation of V<sub>2</sub>CT<sub>x</sub>/V<sub>3</sub>O<sub>7</sub> heterojunctions, the presence of defects in MXene, and the high surface area after oxidation [91].

Urchin-like V<sub>2</sub>CT<sub>x</sub>/V<sub>2</sub>O<sub>5</sub> MXene were produced by hydrothermal synthesis of V<sub>2</sub>CT<sub>x</sub> MXenes at 90 °C/5 days, followed by transformation into urchin-like V<sub>2</sub>CT<sub>x</sub>/V<sub>2</sub>O<sub>5</sub> by subsequent annealing at 450 °C. The sensor exhibited an almost three-times higher response to 15 ppm acetone than pristine V<sub>2</sub>CT<sub>x</sub> MXene at RT. The presence of H-bonds in V<sub>2</sub>CT<sub>x</sub> MXene, a high surface area with an urchin-like morphology, synergistic effects between the V<sub>2</sub>C and V<sub>2</sub>O<sub>5</sub> MXene sensors, and high charge-carrier transport in MXene accounted for the enhanced gas response [92].

In contrast to previous studies on oxidized MXenes, in which oxidation was carried out on assembled films, MXene flakes were oxidized in an aqueous solution to decorate them with oxides and to form maximal Schottky barriers after the process. The sensor, oxidized for 8 h, displayed a response of 175% ( $(|R_g - R_a|)/R_a \times 100$ ) to 5 ppm NO<sub>2</sub> gas at RT. The formation of interflake Schottky barriers in the TiO<sub>2</sub>/Ti<sub>3</sub>C<sub>2</sub> system has been reported as the main reason for the improved gas response [93]. The oxidation of the Ti<sub>2</sub>CT<sub>x</sub> MXenes was investigated at different temperatures (20–447 °C). At 316 °C, oxidation of Ti<sub>2</sub>CT<sub>x</sub> MXene started, and at 447 °C it was completely oxidized to TiO<sub>2</sub>. The sample

oxidized at 316 °C showed better sensing performance relative to the pristine sample. It exhibited the highest response of 61% ( $(|R_g - R_a|)/R_a \times 100$ ) to 100 ppm NH<sub>3</sub> gas at RT. However, their selectivity for NH<sub>3</sub> gas is poor. The increase in the sensing response was attributed to the formation of p-n heterojunctions at the Ti<sub>2</sub>C<sub>2</sub>T<sub>x</sub>/TiO<sub>2</sub> interface. At higher temperatures ( $T > 350$  °C), MXene was not stable. Therefore, MXene sensors are better suited for use at low temperatures [94].

Ti<sub>3</sub>C<sub>2</sub>T<sub>x</sub> MXene/ZnO nanorod (NR) composite synthesized by a chemical route with a surface area of 146.8 m<sup>2</sup>/g showed a very high response of 346% ( $(|R_g - R_a|)/R_a \times 100$ ) to 0.2 ppm NO<sub>2</sub> at RT under UV light, and its  $t_{res}$  and  $t_{rec}$  were 17 and 24 s to 50 ppb NO<sub>2</sub>, respectively. Both MXene and ZnO were photoexcited under UV illumination. The photogenerated electrons in ZnO led to an expansion of the conduction paths inside the ZnO NRs. Moreover, metallic Ti<sub>3</sub>C<sub>2</sub>T<sub>x</sub> MXene served as an electron collector with the formation of Ohmic junctions and further contributed to the generation and separation of photocarriers in the ZnO NRs. Hence, more free carriers were available for gas-sensing reactions under UV irradiation. These photogenerated electrons were abstracted by NO<sub>2</sub> gas, resulting in more remarkable variations in the conduction path width compared with the case of the hybrid. Furthermore, the mesoporous structure of the sensor provides many adsorption sites and gas-diffusion channels for NO<sub>2</sub> gas [95].

A Ti<sub>3</sub>C<sub>2</sub>T<sub>x</sub>-ZnO NS composite was fabricated using a simple sonication approach for 30 min at a power of 100 W. The sensor displayed a high response of 367.63% ( $(|R_g - R_a|)/R_a \times 100$ ) to 20 ppm NO<sub>2</sub> at RT under UV illumination. The large surface area of the gas sensor (9.70 m<sup>2</sup>/g) resulting from its 2D morphology and surface groups of Ti<sub>3</sub>C<sub>2</sub>T<sub>x</sub> along ZnO oxygen vacancies provided numerous adsorption sites for NO<sub>2</sub> gas. Furthermore, the formation of Schottky junctions between Ti<sub>3</sub>C<sub>2</sub>T<sub>x</sub> and ZnO NSs and the photogenerated charge carriers of ZnO under UV light resulted in interactions between NO<sub>2</sub> and ZnO NSs. Based on DFT calculations, the main adsorption sites for NO<sub>2</sub> were on the ZnO NSs, and Ti<sub>3</sub>C<sub>2</sub>T<sub>x</sub> acted as a conductive path to accelerate the flow of charges, resulting in the fast dynamics of the gas sensor [96].

In situ growth of (001) TiO<sub>2</sub> onto 2D Ti<sub>3</sub>C<sub>2</sub>T<sub>x</sub> MXene was performed using hydrothermal synthesis at 160 °C/2–16 h for sensing studies. Under UV light, the sensor prepared from the composites treated for 2 h showed ~34 times more response to 30 ppm NH<sub>3</sub> than that of pristine Ti<sub>3</sub>C<sub>2</sub>T<sub>x</sub>. UV light excited electron-hole pairs on the surfaces of (001) TiO<sub>2</sub> and Ti<sub>3</sub>C<sub>2</sub>T<sub>x</sub>; hence, more electrons and holes were available for sensing in the reactions. TiO<sub>2</sub> with a highly active (001) crystal plane provided efficient photogeneration under UV light, while Ti<sub>3</sub>C<sub>2</sub>T<sub>x</sub> stored holes through the Schottky junction with TiO<sub>2</sub>, which increased the separation of electron-hole pairs, thereby improving the NH<sub>3</sub> sensing performance. In addition, an integrated circuit alarm system was designed to successfully detect the decay process of fresh fish (Figure 10a–d) [97].

The ZnSnO<sub>3</sub>/Ti<sub>3</sub>C<sub>2</sub>T<sub>x</sub> MXene composite hydrothermally synthesized at 150 °C for 24 h exhibited a high response of 194.7% ( $(|R_g - R_a|)/R_a \times 100$ ) towards formaldehyde gas at RT with fast  $t_{res}$  and  $t_{rec}$  of 6.2 s and 5.1 s, respectively. The surface area of pristine ZnSnO<sub>3</sub> was 20.62 m<sup>2</sup>/g, and it was increased to 28.39 m<sup>2</sup>/g for the composite sample, where ZnSnO<sub>3</sub> nanocubes were uniformly dispersed on Ti<sub>3</sub>C<sub>2</sub>T<sub>x</sub> MXene NSs. In addition, the functional groups on the Ti<sub>3</sub>C<sub>2</sub>T<sub>x</sub> MXene NSs provided numerous active sites for the adsorption of formaldehyde molecules. The formation of heterojunctions at the interface between ZnSnO<sub>3</sub> and Ti<sub>3</sub>C<sub>2</sub>T<sub>x</sub> MXene was attributed to the modulation of the resistance. In addition, the fast dynamics are related to the high charge mobility of MXene [98].

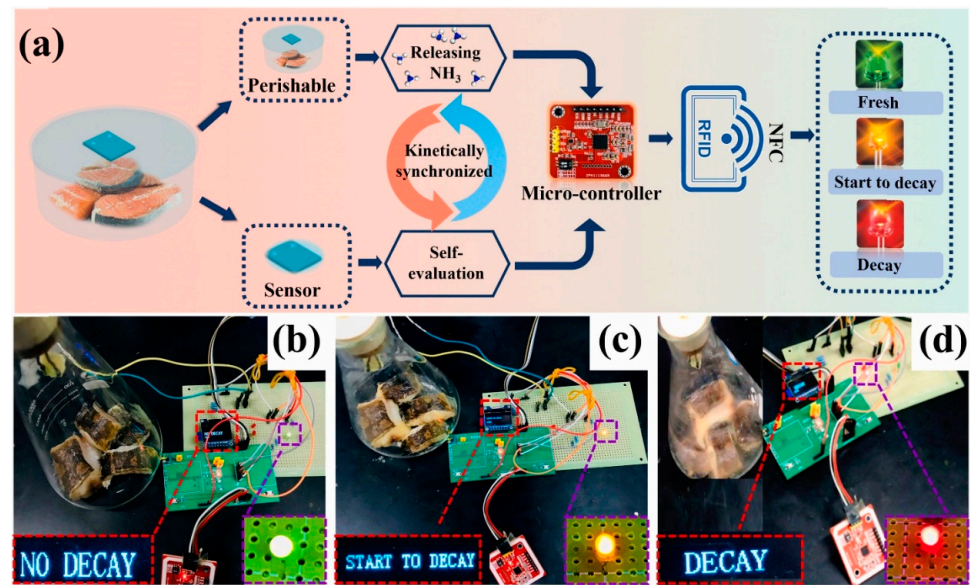


**Figure 10.** (a) Block diagram of the integrated circuit alarm system. Monitoring the fish status of (b) no decay, (c) start to decay, and (d) decay [97]. With permission from Elsevier.

### 2.2.2. MXene-TMD Composites

Two-dimensional transition metal dichalcogenides (TMDs) have high surface areas, abundant adsorption sites, and high surface reactivities; therefore, their composites with MXenes are promising for sensing studies [99,100]. In a relevant study, a  $\text{Ti}_3\text{C}_2\text{T}_x\text{-WSe}_2$  composite was chemically prepared and the fabricated sensor displayed a response of 9%  $([(R_g - R_a) / R_a] \times 100)$  to 40 ppm ethanol at RT. In addition, fast  $t_{\text{res}}$  (9.7 s) and  $t_{\text{rec}}$  (6.6 s) were recorded. The enhanced response to ethanol gas is related to the numerous heterojunctions generated between  $\text{Ti}_3\text{C}_2\text{T}_x$  and  $\text{WSe}_2$ . The enhanced response to ethanol gas is related to the numerous heterojunctions generated between  $\text{Ti}_3\text{C}_2\text{T}_x$  and  $\text{WSe}_2$ . In heterojunctions, band bending occurs, and as a result, potential barriers will be formed between two materials, leading to difficulty of flow of the charge carriers. Upon injection of the target gas, the height of potential barriers changes, contributing to significant resistance changes in heterojunctions. More heterojunctions result in higher modulation of the sensor resistance. In addition, after 1000 bending cycles, the performance not only did not decrease, but also slightly increased owing to the creation of microcracks and wrinkles by the strain forces, which acted as adsorption sites [101].

The influence of the electrode type on sensing performance was explored. A flexible paper-based sensor using a  $\text{Ti}_3\text{C}_2\text{T}_x/\text{WS}_2$  composite was fabricated using either a  $\text{Ti}_3\text{C}_2\text{T}_x\text{-MXene}$  electrode (ME) or a Au electrode (AE). The ME +  $\text{Ti}_3\text{C}_2\text{T}_x/\text{WS}_2$  gas sensor exhibited the highest response of 15.2%  $([(R_g - R_a) / R_a] \times 100)$  to 1 ppm  $\text{NO}_2$  gas at RT, owing to the formation of Ohmic contact between the sensing layer and ME, in contrast to the Schottky contact formed between the sensor and AE. When Au and  $\text{Ti}_3\text{C}_2\text{T}_x/\text{WS}_2$  were in contact, the formation of Schottky potential barriers prevented the transport of charges between the two materials, and only a small number of carriers were able to cross the junction. In contrast, when  $\text{Ti}_3\text{C}_2\text{T}_x/\text{WS}_2$  contacted the ME, the height of the barrier between the nonmetal ME and the  $\text{Ti}_3\text{C}_2\text{T}_x/\text{WS}_2$  sensor was much lower, which allowed the easy transport of charge carriers across the junction. Furthermore, the flexible 2D ME has a large specific surface area and offers adequate adsorption and reaction sites for oxygen and the target gas. In addition, numerous surface groups are present on the ME surface, which affect the sensing performance. Finally, the excellent conductivity of  $\text{Ti}_3\text{C}_2\text{T}_x$  accelerated the electron flow during the sensing process and shortened  $t_{\text{rec}}$ . The optimized sensor showed good flexibility by maintaining its performance even after bending 500 times by  $60^\circ$  [102]. A  $\text{MoS}_2/\text{Ti}_3\text{C}_2\text{T}_x$  composite was prepared using a hydrothermal method [103]. The SEM

micrographs of the components and composite are shown in Figure 11a–d.  $\text{Ti}_3\text{AlC}_2$  exhibits a laminated structure. After etching in HF, the morphology of  $\text{Ti}_3\text{C}_2\text{T}_x$  MXene comprised an accordion-like structure (Figure 11b). The  $\text{MoS}_2$  sample showed a nanoflower morphology (Figure 11c). Moreover, Figure 11d shows that the  $\text{MoS}_2$  nanoflowers were on and between the  $\text{Ti}_3\text{C}_2\text{T}_x$  interlayers, forming a 3D interconnected network structure with high surface areas, which is beneficial for gas-sensing applications.

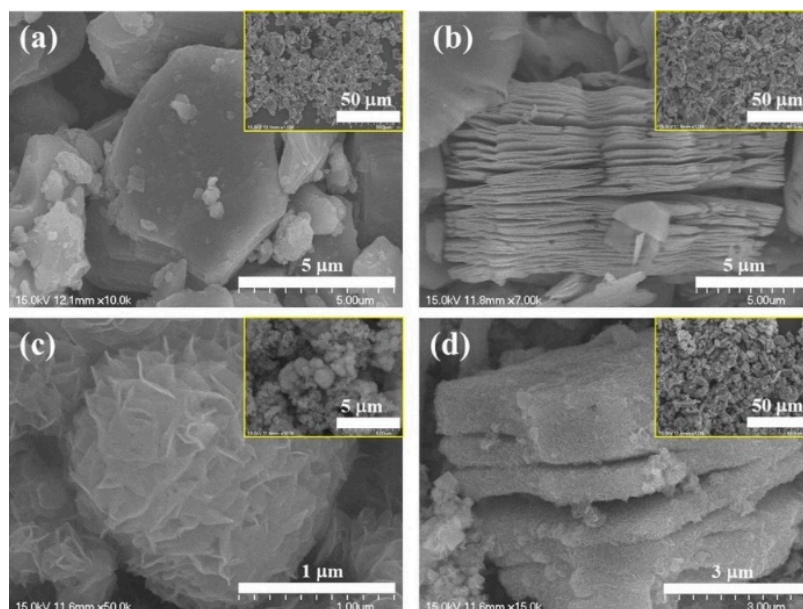


**Figure 11.** SEM images of (a)  $\text{Ti}_3\text{AlC}_2$  powder, (b)  $\text{Ti}_3\text{C}_2\text{T}_x$  MXene, (c)  $\text{MoS}_2$  nanoflower, and (d)  $\text{MoS}_2/\text{Ti}_3\text{C}_2\text{T}_x$  composite. Inset shows higher magnification images [103]. With permission from Elsevier.

The sensor exhibited a response of 45% ( $(|R_g - R_a|)/R_a \times 100$ ) to 20 ppm  $\text{NH}_3$  gas at RT. The specific surface area of  $\text{MoS}_2/\text{Ti}_3\text{C}_2\text{T}_x$  ( $23.5 \text{ m}^2/\text{g}$ ) was enhanced relative to pristine counterparts due to the small flake size and template-conformable  $\text{MoS}_2$  NSs, which enhanced the amount of active sites and increased the flow of electrons. The formation of  $\text{MoS}_2\text{-Ti}_3\text{C}_2\text{T}_x$  MXene heterojunctions and the presence of a large number of S- and Mo-terminated edges enhanced the interaction of  $\text{NO}_2$  gas with the sensing material. Based on DFT calculations, the adsorption of  $\text{NO}_2$  was more favorable than that of other gases owing to its large adsorption energy, leading to an enhanced response of the sensing device to  $\text{NO}_2$  gas [103].

The Etched  $\text{MoS}_2$  NSs were grown on  $\text{Ti}_3\text{C}_2\text{T}_x$  MXene via hydrothermal synthesis at  $210^\circ\text{C}$  for 18 h (Figure 12). The composite sensor exhibited a high response of 65.6% ( $(|R_g - R_a|)/R_a \times 100$ ) to 100 ppm  $\text{NO}_2$  gas at RT, which is higher than that of  $\text{MoS}_2$ . The composite with a 3D uniform morphology had a large number of active sites. Furthermore, the sensing response is attributed to the presence of fast channels for carrier flow between  $\text{MoS}_2$  and  $\text{Ti}_3\text{C}_2\text{T}_x$  MXene [104].

$\text{Ti}_3\text{C}_2\text{T}_x/\text{WS}_2$  nanocomposites with different amounts of  $\text{WS}_2$  were prepared using a simple chemical route for  $\text{NO}_2$  sensing. The response to  $\text{NO}_2$  depended on the amount of  $\text{WS}_2$  in the composite, and the sensor with 50%  $\text{WS}_2$  in the composite revealed the best response of 55.6% ( $(|R_g - R_a|)/R_a \times 100$ ) to 2 ppm  $\text{NO}_2$  gas at RT under visible light, which was  $\sim 3.2$  times higher than that under the dark conditions (17.4%). The metal-like conductivity of MXene improves the separation and transfer of photogenerated electron-hole pairs. In addition, the large contact areas of the 2D/2D heterostructures improved the carrier transportation under light illumination. However, the response decreases gradually, because the photogenerated carriers are captured by the defects inside and at the interfaces

between the two materials, leading to the recombination of electrons and holes and a decrease in the sensing performance [105].

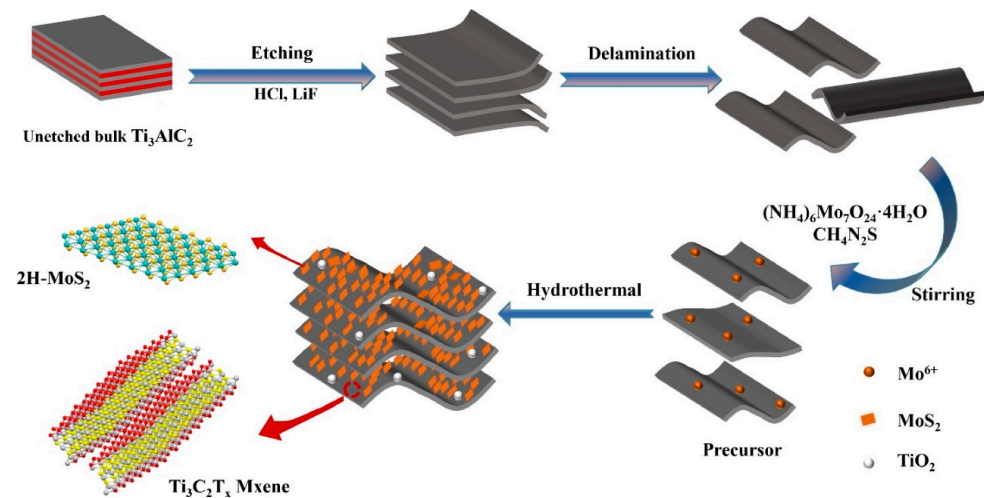


**Figure 12.** Schematic synthesis procedure of MoS<sub>2</sub> NSs-Ti<sub>3</sub>C<sub>2</sub>T<sub>x</sub> MXene nanocomposite [104]. With permission from Elsevier.

Both Ti<sub>3</sub>C<sub>2</sub>T<sub>x</sub>-WO<sub>3</sub> (10, 20, and 30 wt%) and Ti<sub>3</sub>C<sub>2</sub>T<sub>x</sub>-MoS<sub>2</sub> (10, 20, and 30 wt%) composites were fabricated using hydrothermal synthesis at 170 °C for 8 h, for NO<sub>2</sub> gas sensing studies at RT. The initial Ti<sub>3</sub>AlC<sub>2</sub> MAX phase exhibited densely layered structures (Figure 13a). After HF etching, the Ti<sub>3</sub>C<sub>2</sub> MXene exhibited an accordion-like morphology (Figure 13b). Figure 13c shows the morphology of MoS<sub>2</sub>. Figure 13d shows the morphology of the Ti<sub>3</sub>C<sub>2</sub>-MoS<sub>2</sub> composite, in which MoS<sub>2</sub> is located on both the surface and the interlayers of Ti<sub>3</sub>C<sub>2</sub>, reflecting intimate contacts between them. The Ti<sub>3</sub>C<sub>2</sub>-MoS<sub>2</sub> composite sensor showed a response of 35.8% ( $[(|R_g - R_a|)/R_a] \times 100$ ) to 10 ppm NO<sub>2</sub> gas at RT, and overall, the responses of Ti<sub>3</sub>C<sub>2</sub>-MoS<sub>2</sub> composites to NO<sub>2</sub> gas were higher than those of Ti<sub>3</sub>C<sub>2</sub>-WO<sub>3</sub> composites. However, the high amount of MoS<sub>2</sub> (30 wt%) in the composite limited the number of adsorption sites on MXene, causing a decrease in the gas response. The formation of heterojunctions between MoS<sub>2</sub> and MXene, along with the presence of numerous surface groups on MXene, contributed to the sensor response [106].

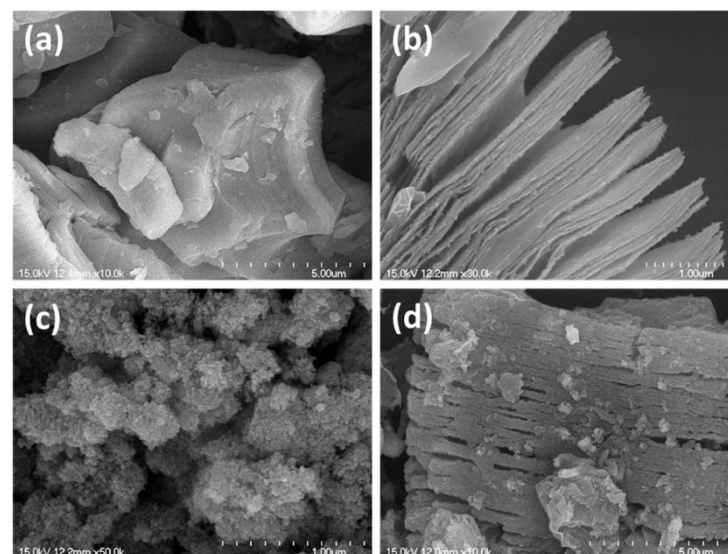


**Figure 13.** SEM images of (a) Ti<sub>3</sub>AlC<sub>2</sub>, (b) Ti<sub>3</sub>C<sub>2</sub> MXene, (c) MoS<sub>2</sub>, and (d) Ti<sub>3</sub>C<sub>2</sub>-MoS<sub>2</sub> [106]. With permission from Elsevier.

### 2.2.3. MXene-Conducting Polymers Composites

Conducting polymers (CPs) are promising materials for gas sensors because of their high conductivity, possibility of working at RT, tunable chemical composition, easy doping, and low price [107–109]; therefore, they can be used with MXene to boost the RT gas-sensing properties of the resultant composite. A sensor was fabricated for RT ammonia sensing by the in situ polymerization of PEDOT and PSS on  $\text{Ti}_3\text{C}_2\text{T}_x$  MXene. The sensor showed a high response of 36.6% ( $(|R_g - R_a|)/R_a \times 100$ ) to 100 ppm of  $\text{NH}_3$  with  $t_{\text{res}}$  and  $t_{\text{rec}}$  of 2 min and 40 s, respectively. In addition, the sensor on the flexible PI substrate exhibited good mechanical flexibility by maintaining its performance at different bending angles. Charge flow occurred between the  $\text{NH}_3$  molecules and the sensor surface, leading to a change in the electrical conductivity. Furthermore, the high specific surface area of the composite, along with  $\pi = \pi$  interactions, increased the concentration of charge carriers [110].

A  $\text{Ti}_3\text{C}_2\text{T}_x$  MXene/urchin-like polyaniline (PANI) composite was produced using a template method by employing sulfonated PS nanosphere templates and in situ polymerization on flexible polyethylene terephthalate (PET). The sensor disclosed a high response of 3.70 to 10 ppm  $\text{NH}_3$  at RT, which was higher than that of the pristine sensor. The enhanced sensing was related to the hollow urchin-like morphology of PANI and the NS morphology of  $\text{Ti}_3\text{C}_2\text{T}_x$ , both of which were beneficial for providing more adsorption sites for  $\text{NH}_3$  gas. Second, Schottky heterojunctions were generated by the intimate contact between PANI and the  $\text{Ti}_3\text{C}_2\text{T}_x$  NS, which shortened the diffusion length for charges and led to fast charge flow. Furthermore, the degree of protonation of PANI increased through its connection with the  $\text{Ti}_3\text{C}_2\text{T}_x$  NS. The increased  $-\text{NH}_2^+$  and  $=\text{NH}^+$  groups in the composite led to an enhanced response to  $\text{NH}_3$  gas. As  $\text{NH}_3$  is an indicator of meat freshness, the fabricated sensor was successfully used to evaluate pork meat freshness. After 36 h, the sensor was able to indicate an increase in  $\text{NH}_3$  concentration in the meat, confirming spoilage [111]. PANI NPs were decorated with  $\text{Ti}_3\text{C}_2\text{T}_x$  NSs via in situ polymerization. The sensor displayed a response ( $\Delta I/I_0$ ) of 40 to 200 ppm ethanol gas at RT. In addition, it exhibited good mechanical flexibility; under bending from  $0^\circ$  to  $120^\circ$ , it exhibited almost the same performance, demonstrating good flexibility. In particular, under bending to  $\sim 120^\circ$  it showed a high response of 27.4% ( $(|R_g - R_a|)/R_a \times 100$ ) to 150 ppm ethanol. In addition, the  $t_{\text{res}}$  and  $t_{\text{rec}}$  were 0.6 and 0.8 s, respectively, after bending. Based on DFT calculations, the adsorption energies of  $-0.985$ ,  $-0.689$ , and  $-0.544$  were calculated for OH-terminated  $\text{Ti}_3\text{C}_2$ , O-terminated  $\text{Ti}_3\text{C}_2$ , and F-terminated  $\text{Ti}_3\text{C}_2$ , respectively. This demonstrates that the OH-terminated  $\text{Ti}_3\text{C}_2$  had the strongest binding energy for ethanol [112].

A  $\text{Ti}_3\text{C}_2\text{T}_x$  composite with conjugated polymers (poly[3,6-diamino-10-methylacridinium chloride-co-3,6-diaminoacridine-squaraine], PDS-Cl) and polarly charged nitrogen was used for  $\text{H}_2\text{S}$  gas sensing. The sensor with 10 wt% MXene exhibited a response of 2% ( $(|R_g - R_a|)/R_a \times 100$ ) to 5 ppm  $\text{H}_2\text{S}$  at RT. Charge transfer-induced modifications in carrier density are responsible for  $\text{H}_2\text{S}$  gas sensing. By opening the interlayer spaces of MXene by the polymer, the number of accessible active sites increased and intercalation became easier, leading to an enhancement of the charge-transfer effect. Furthermore, the MXene surfaces contain numerous surface groups that have a remarkable effect on gas adsorption [113].

Cationic polyacrylamide (CPAM) with abundant surface groups can form hydrogen bonds with  $\text{NH}_3$ , enhancing its response to this gas. The CPAM/ $\text{Ti}_3\text{C}_2\text{T}_x$  MXene composite was prepared for gas sensing at RT. The sensor displayed a response of 25% ( $(|R_g - R_a|)/R_a \times 100$ ) to 100 ppm  $\text{NH}_3$  gas at RT. In addition, under bending conditions, the sensor performance did not change significantly, and under the bent state ( $60^\circ$ ) for 140 cycles, the sensor still showed no degradation in performance. With an increase in the bending angle, the current of the CPAM/ $\text{Ti}_3\text{C}_2\text{T}_x$  sensor was slightly reduced because of the presence of CPAM, which allowed the  $\text{Ti}_3\text{C}_2\text{T}_x$  NSs to bond together and show good flexibility [114].

### 2.2.4. Ternary Composites

MXene-based ternary composites have been studied less for gas-sensing applications than binary composites because of the complexity of the synthesis procedure and the need for optimization of the three components. However, they exhibit superior sensing properties because there are more resistance-modulation sources inside the sensing materials.

A hamburger-like SnO-SnO<sub>2</sub>/Ti<sub>3</sub>C<sub>2</sub>T<sub>x</sub> MXene nanocomposite was hydrothermally prepared at 120 °C for 8 h. It revealed a high response of 12.1 to 100 ppm acetone at RT, which was higher than that of the pristine sensors. Moreover, it revealed a  $t_{\text{rec}}$  of 9 s. The improved response was related to the higher surface area of the SnO-SnO<sub>2</sub>-Ti<sub>3</sub>C<sub>2</sub>T<sub>x</sub> MXene composite (46.7 m<sup>2</sup>/g), relative to pristine Ti<sub>3</sub>C<sub>2</sub>T<sub>x</sub> (13.6 m<sup>2</sup>/g), and SnO-SnO<sub>2</sub> (38.6 m<sup>2</sup>/g) gas sensors. Furthermore, there are more resistance modulation sources in the nanocomposite than in the other sensors. Figure 14a shows the energy levels of the SnO-SnO<sub>2</sub>/Ti<sub>3</sub>C<sub>2</sub>T<sub>x</sub> sensor components before contact, showing different work functions of these materials. Upon intimate contact, the electrons move from MXene and SnO<sub>2</sub> to SnO to equate the Fermi levels (Figure 14b,c). This leads to the formation of a hole accumulation layer (HAL) and an electron depletion layer (EDL) on the MXene and SnO<sub>2</sub> sides, respectively [115]. In an acetone atmosphere (Figure 3d), narrowing of both the HAL and EDL led to the modulation of the sensor resistance, contributing to the sensing feedback.

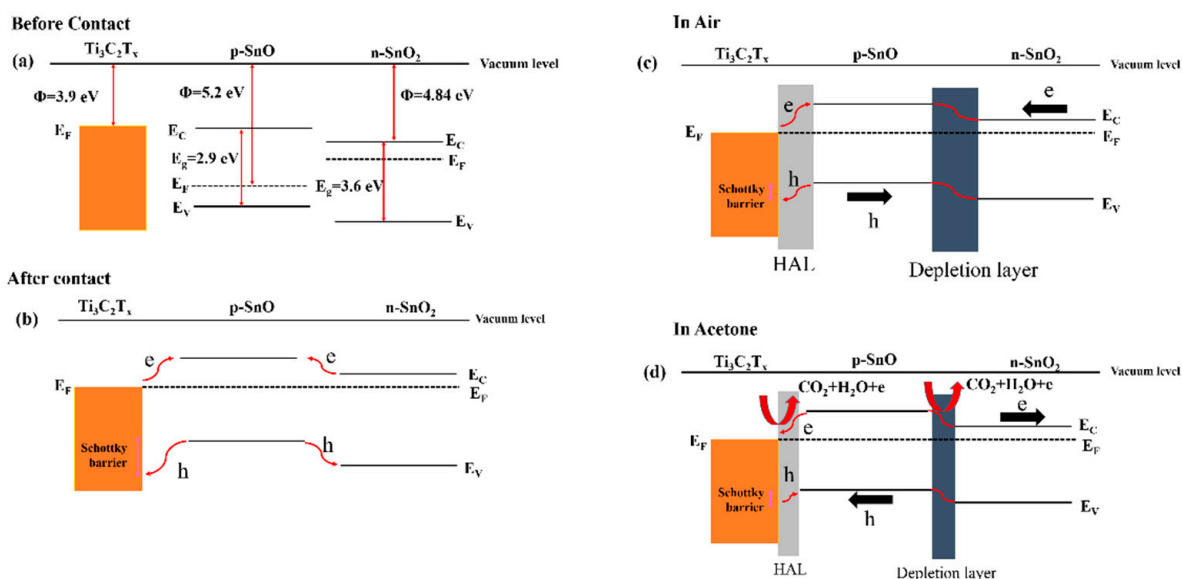


**Figure 14.** Schematic of the band structure in SnO-SnO<sub>2</sub>/Ti<sub>3</sub>C<sub>2</sub>T<sub>x</sub> nanocomposite (a) before and (b) after contact in (c) air and (d) acetone [115]. With permission from Elsevier.

A Ti<sub>3</sub>C<sub>2</sub>T<sub>x</sub> MXene composited with a marigold flower-like V<sub>2</sub>O<sub>5</sub>/CuWO<sub>4</sub> heterojunction was hydrothermally synthesized at 180 °C/12 h for NH<sub>3</sub> gas sensing (Figure 15). It showed a high response of 53.5 to 51 ppm NH<sub>3</sub> at RT with  $t_{\text{res}}$  and  $t_{\text{rec}}$  of 100 and 115 s, respectively. After contact of the Ti<sub>3</sub>C<sub>2</sub>T<sub>x</sub> MXene with V<sub>2</sub>O<sub>5</sub>/CuWO<sub>4</sub> in air, a Schottky barrier was formed (Figure 15). Therefore, electrons flowed from n-type V<sub>2</sub>O<sub>5</sub>/CuWO<sub>4</sub> to MXene. In addition, MXene acted as a pathway for electrons to move through Ti<sub>3</sub>C<sub>2</sub>T<sub>x</sub>/V<sub>2</sub>O<sub>5</sub>/CuWO<sub>4</sub> more easily than through V<sub>2</sub>O<sub>5</sub>/CuWO<sub>4</sub>, and the modulation of the barrier height in the NH<sub>3</sub> gas contributed to the sensing mechanism. Moreover, Ti<sub>3</sub>C<sub>2</sub>T<sub>x</sub> MXene facilitates electron flow to the electrodes [116].

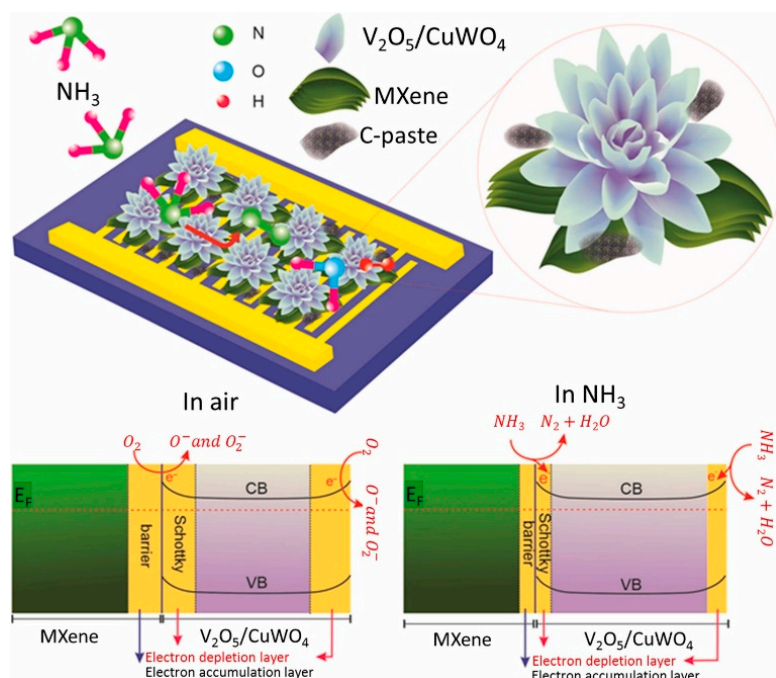


**Figure 15.**  $\text{NH}_3$ -sensing mechanism of  $\text{Ti}_3\text{C}_2\text{T}_x/\text{V}_2\text{O}_5/\text{CuWO}_4$  sensor [116]. With permission from Elsevier.

Ternary 2D  $\text{Ti}_3\text{C}_2\text{T}_x$  MXene@ $\text{TiO}_2/\text{MoS}_2$  composites were prepared using the hydrothermal method for  $\text{NH}_3$  sensing at RT. It showed a response of 164% ( $[(|R_g - R_a|)/R_a] \times 100$ ) to 100 ppm  $\text{NH}_3$  gas at RT, which was higher than that of the pristine sensor counterparts. The improved sensing of  $\text{NH}_3$  was attributed to the layered nanostructure with a unique morphology and p-n heterojunctions. Furthermore, DFT studies indicated that  $\text{NH}_3$  was able to transfer more charge to the composite surface than to pristine  $\text{Ti}_3\text{C}_2\text{T}_x$  MXene and  $\text{MoS}_2$ , resulting in a higher modulation of the resistance [117].

A 2D  $\text{Ti}_3\text{C}_2\text{T}_x$  MXene- $\text{MoO}_2/\text{MoO}_3$  NSs composite was fabricated using the hydrothermal method at  $180^\circ\text{C}/10\text{ h}$  for ethanol detection at RT. It revealed a high response of 19.77 to 200 ppm to ethanol, and fast  $t_{\text{res}}$  and  $t_{\text{rec}}$  (46 s/276 s). The high surface area ( $13.54\text{ m}^2/\text{g}$ ) and abundant surface groups on MXene provided more active sites for the adsorption of oxygen and ethanol molecules. Furthermore, as revealed in Figure 16a–d, the generated p-n and n-n heterojunctions remarkably improved the carrier migration rate and shortened  $t_{\text{res}}$  and  $t_{\text{rec}}$ . MXene,  $\text{MoO}_2$  and  $\text{MoO}_3$  have different work functions of 3.9, 6.5 and 2.9 eV, respectively. When they are contacted, the electrons move from MXene and  $\text{MoO}_3$  to  $\text{MoO}_2$  to equate the Fermi levels inside of contacts. This results in formation of Schottky barriers in interfaces between MXene and  $\text{MoO}_2$  and n-n heterojunctions at interfaces between  $\text{MoO}_2$  and  $\text{MoO}_3$  in air. When the sensor is exposed to ethanol, the electrons are released back to the sensor surface and the height of Schottky barriers and heterojunctions decreases, which finally lead to the resistance modulation of the sensor. Finally, the electrical conductivity of MXene decreases the resistance and sensing temperature [118].

Various nanocomposites such as MXenes with GO, ZnO, CuO, GO/ZnO, GO/CuO, ZnO/CuO, and GO/ZnO/CuO have been hydrothermally synthesized for  $\text{NH}_3$  sensing at RT. Among them,  $\text{Ti}_3\text{C}_2\text{T}_x$  MXene/GO/CuO/ZnO with an optimal ratio of 9:1:5:5 exhibited the best  $\text{NH}_3$  gas sensing without resistance drift. The response to 200 ppm was 96% ( $[(|R_g - R_a|)/R_a] \times 100$ ) along with good humidity independence. The improved sensing response was related to the generation of multiple p-n and p-p heterojunctions, as well as the presence of many functional groups on the surfaces of MXene and GO [119].

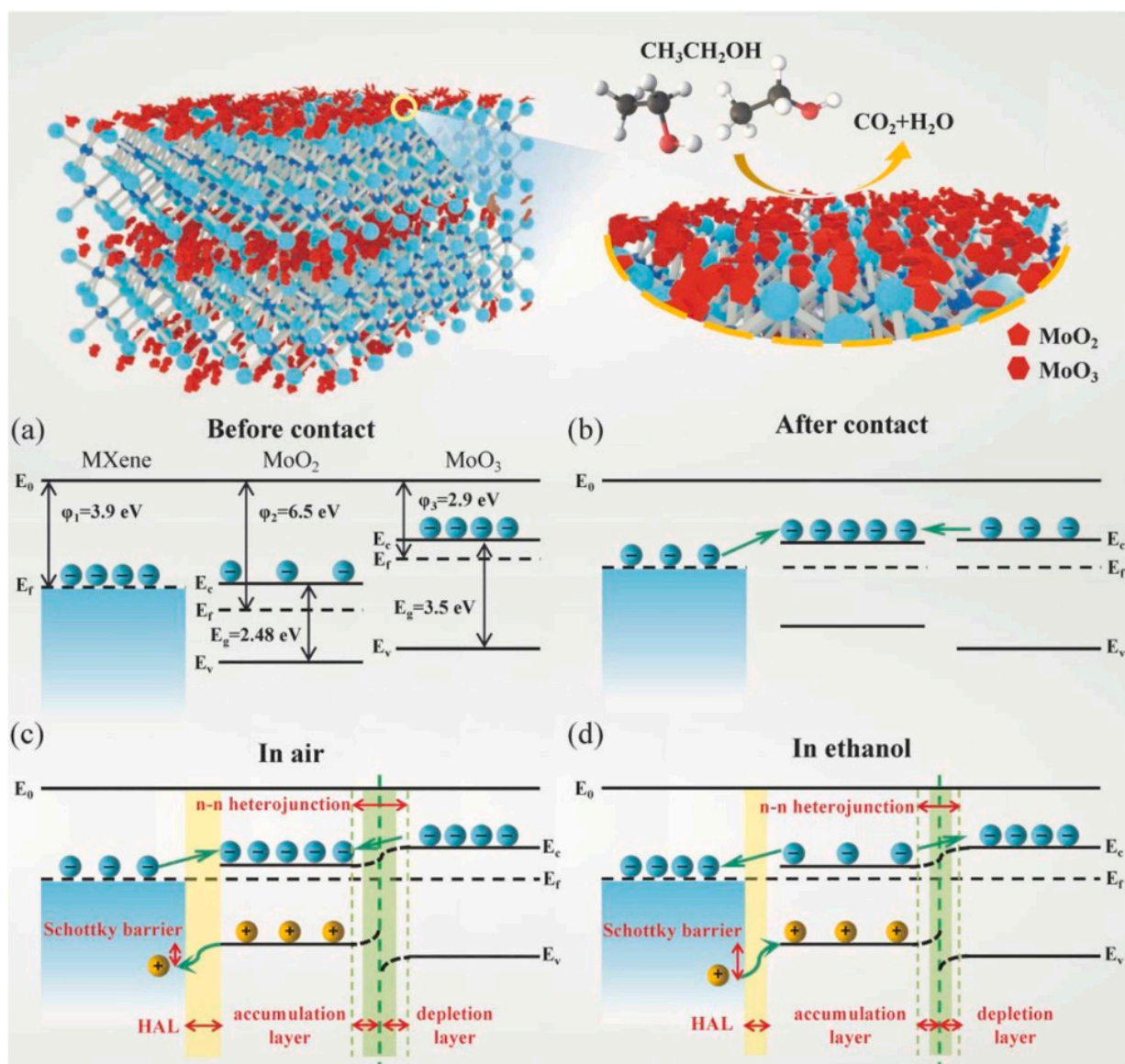


**Figure 16.** (a–d) Schematic of the gas-sensing mechanism of MoO<sub>2</sub>/MoO<sub>3</sub>/MXene-based sensor [118]. With permission from Elsevier.

A 3D Ti<sub>3</sub>C<sub>2</sub>T<sub>x</sub> MXene/rGO/SnO<sub>2</sub> aerogel was fabricated using a facile solvothermal approach at 140 °C for 24 h. It exhibited a response of 54.97%  $\left(\frac{|R_g - R_a|}{R_a}\right) \times 100$  to 10 ppm formaldehyde at RT. In addition, it indicated short  $t_{res}$  and  $t_{rec}$  (2.9 and 2.2 s) along with high stability. The high surface area of 103 m<sup>2</sup>/g and the generation of p-n junctions between rGO and SnO<sub>2</sub> and p-p junctions between MXene and rGO contributed to the sensing mechanism. Based on DFT calculations, the adsorption energy of HCHO on Ti<sub>3</sub>C<sub>2</sub>T<sub>x</sub> MXene/rGO/SnO<sub>2</sub> was −5.7 eV, which was larger than that for other sensors [120].

### 2.2.5. Other MXene-Based Composites

A hollow nanofiber GaN/Ti<sub>3</sub>C<sub>2</sub>T<sub>x</sub> composite was synthesized by hydrothermal nitridation at 120 °C/12 h. Ti<sub>3</sub>C<sub>2</sub>T<sub>x</sub>, which has metallic properties, acts as a conductive channel and decreases the overall resistance at RT. In addition, Ti<sub>3</sub>C<sub>2</sub>T<sub>x</sub> accelerated charge flow during the sensing reactions, resulting in fast sensor dynamics at RT. Accordingly, the response of the composite sensor to 50 ppm NH<sub>3</sub> was 3.5 times higher than that of the bare Ti<sub>3</sub>C<sub>2</sub>T<sub>x</sub>. The large specific surface area and unique hollow porous morphology of the GaN NFs provide sufficient adsorption sites for NH<sub>3</sub> gas. The formation of p-n

$\text{Ti}_3\text{C}_2\text{T}_x$ -GaN heterojunctions is beneficial for resistance modulation. The responses to  $\text{NH}_3$  were not affected by 20–80%RH. At high humidity, the sensor was covered with multilayered physisorbed water, leading to the inhibition of the direct reaction between the adsorbed oxygen and  $\text{NH}_3$  [121].

$\text{Ni}(\text{OH})_2$  has features such as non-toxicity, low cost, ease of synthesis, and semiconducting properties.  $\text{Ni}(\text{OH})_2/\text{Ti}_3\text{C}_2\text{T}_x$  composites were synthesized via in situ electrostatic self-assembly. The sensor with ~7.8 wt%  $\text{Ni}(\text{OH})_2$  revealed the highest response, of 13%  $([(|R_g - R_a|)/R_a] \times 100)$  to 50 ppm  $\text{NH}_3$  gas at RT. A further increase in  $\text{Ni}(\text{OH})_2$  resulted in the partial aggregation of  $\text{Ni}(\text{OH})_2$ , causing a decrease in the number of adsorption sites and the sensing response. The formation of interfacial Schottky junctions between the two components and the increase in adsorption sites owing to the high surface area ( $54 \text{ m}^2/\text{g}$ ) are attributed to the sensing mechanism [122].

A  $\text{BiOCl}-\text{Ti}_3\text{C}_2\text{T}_x$  MXene composite with an NS morphology, excellent homogeneity, and good electronic characteristics was synthesized for sensing studies. It revealed a high response to 34.58 to 100 ppm  $\text{NO}_2$  gas at 80%RH. The high response of the gas sensor was attributed to the formation of p-p heterojunctions between  $\text{BiOCl}$  and MXene [123].

The  $\text{SnS}_2/\text{Ti}_3\text{C}_2$  MXene composites were produced via electrostatic interactions. The response to 50 ppm acetone was 29.8%  $([(|R_g - R_a|)/R_a] \times 100)$  at RT, and the  $t_{\text{res}}$  and  $t_{\text{rec}}$  were ~90 and 355 s, respectively. The oxygen-containing functional groups on  $\text{Ti}_3\text{C}_2$  formed hydrogen bonds with acetone. Electrons flowed from  $\text{Ti}_3\text{C}_2\text{T}_x$  to  $\text{SnS}_2$  to form heterojunctions with potential barriers, the heights of which were changed upon exposure to target gas. The sensor could detect acetone in both the optical and electrical modes. To demonstrate the optical mode of the sensor, the sensor signal was connected to an LED, and the blue light evolution images of the LED at various acetone concentrations were processed. The brightness of the LED increased with increasing acetone concentration (Figure 17a–d). The brightness of the LED increased with increasing acetone concentration (Figure 17a–d). A favorable correspondence was observed between the Euclidean distance and acetone concentration (1–100 ppm); the Euclidean distance was 109 for 50 ppm acetone [124].

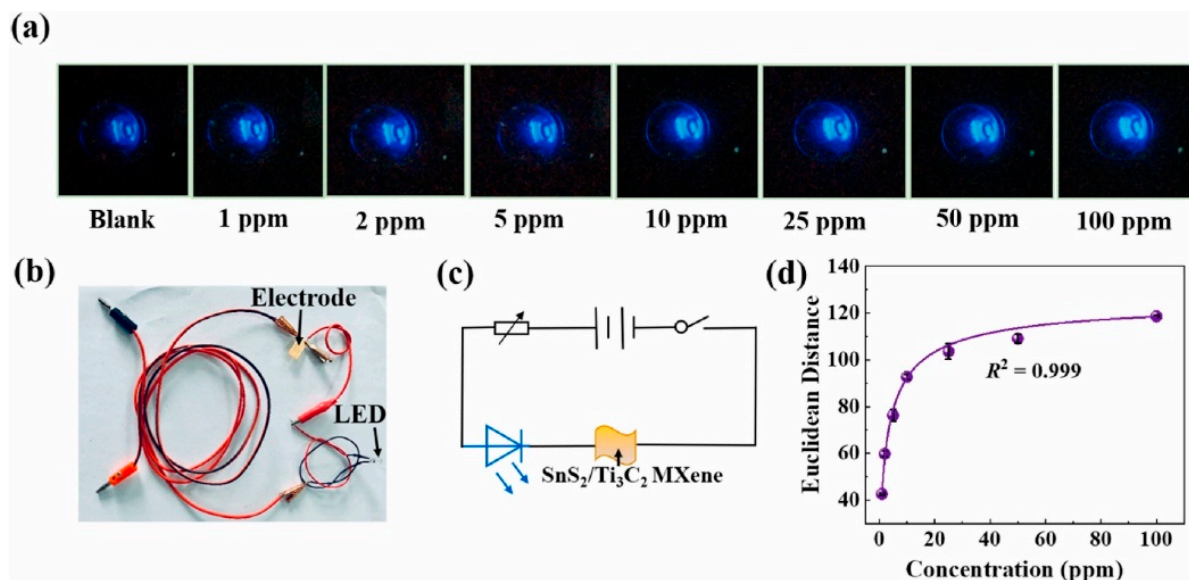


**Figure 17.** (a) Images and light evolutions of  $\text{SnS}_2/\text{Ti}_3\text{C}_2$  MXene-based visual sensor to detect acetone. (b) Photograph and (c) diagram of circuit. (d) The fitted curve of the Euclidean distance with acetone concentration [124]. With permission from Elsevier.

Table 2 presents the RT gas-sensing properties of composite MXene-based gas sensors. They are mostly used for detection of  $\text{NH}_3$ , methanol,  $\text{NO}_2$ , HCHO, ethanol and acetone gases at RT.

**Table 2.** RT gas-sensing properties of composite MXene-based gas sensors.

Sensing Material	Gas	Conc. (ppm)	Response (%) ((( $R_g - R_a$ ) / $R_a$ ) × 100)	Ref.
SnO <sub>2</sub> /Ti <sub>3</sub> C <sub>2</sub> T <sub>x</sub> composite	NH <sub>3</sub>	40	40	[75]
Ti <sub>3</sub> C <sub>2</sub> T <sub>x</sub> -SnO <sub>2</sub> composite	NH <sub>3</sub>	100	3.1	[78]
NiO/Ti <sub>3</sub> C <sub>2</sub> T <sub>x</sub> MXene nanocomposites	NH <sub>3</sub>	50	6.13	[79]
Ti <sub>3</sub> C <sub>2</sub> T <sub>x</sub> MXene (30–100 wt%)/In <sub>2</sub> O <sub>3</sub> composite	NH <sub>3</sub>	20	100	[81]
In <sub>2</sub> O <sub>3</sub> nanocubes/Ti <sub>3</sub> C <sub>2</sub> T <sub>x</sub> MXene composites	Methanol	5	29.6	[83]
Hollow In <sub>2</sub> O <sub>3</sub> microbutes (2–5 μm) were attached on the exfoliated Ti <sub>3</sub> C <sub>2</sub> T <sub>x</sub> MXene	NH <sub>3</sub>	5	60.6	[84]
α-Fe <sub>2</sub> O <sub>3</sub> /Ti <sub>3</sub> C <sub>2</sub> T <sub>x</sub> MXene	Acetone	5	16.6	[85]
Rose-like α-Fe <sub>2</sub> O <sub>3</sub> /Ti <sub>3</sub> C <sub>2</sub> T <sub>x</sub> MXene composite	NH <sub>3</sub>	5	18.3	[86]
Ti <sub>3</sub> C <sub>2</sub> T <sub>x</sub> /WO <sub>3</sub> nanocomposite	NO <sub>2</sub>	0.2	78	[87]
WO <sub>3</sub> —Ti <sub>3</sub> C <sub>2</sub> T <sub>x</sub> nanocomposite	NH <sub>3</sub>	1	22.3	[88]
Ti <sub>3</sub> C <sub>2</sub> T <sub>x</sub> MXene/CuO	NH <sub>3</sub>	5	46.7	[89]
Ti <sub>3</sub> C <sub>2</sub> T <sub>x</sub> /CuO nanocomposites	NO <sub>2</sub>	50	57	[90]
V <sub>2</sub> CT <sub>x</sub> /V <sub>3</sub> O <sub>7</sub> nanocomposites	NO <sub>2</sub>	100	16	[91]
Ti <sub>3</sub> C <sub>2</sub> T <sub>x</sub> MXene/ZnO NRs	NO <sub>2</sub>	0.2	346	[94]
Ti <sub>3</sub> C <sub>2</sub> T <sub>x</sub> -ZnO nanocomposite	NO <sub>2</sub>	20	367.63	[96]
ZnSnO <sub>3</sub> /Ti <sub>3</sub> C <sub>2</sub> T <sub>x</sub> MXene composite	HCHO	100	194.7	[98]
Ti <sub>3</sub> C <sub>2</sub> T <sub>x</sub> -WSe <sub>2</sub> composite	Ethanol	40	9	[101]
MoS <sub>2</sub> /Ti <sub>3</sub> C <sub>2</sub> T <sub>x</sub> composite	NH <sub>3</sub>	20	45	[103]
MoS <sub>2</sub> /Ti <sub>3</sub> C <sub>2</sub> T <sub>x</sub> composite	NO <sub>2</sub>	100	65.6	[104]
Ti <sub>3</sub> C <sub>2</sub> T <sub>x</sub> /WS <sub>2</sub> nanocomposites	NO <sub>2</sub>	2	55.6	[105]
Ti <sub>3</sub> C <sub>2</sub> -MoS <sub>2</sub> composite	NO <sub>2</sub>	10	35.8	[106]
PEDOT and PSS on Ti <sub>3</sub> C <sub>2</sub> T <sub>x</sub> MXene	NH <sub>3</sub>	100	36.6	[110]
PANI NPs Ti <sub>3</sub> C <sub>2</sub> T <sub>x</sub> NSs	Ethanol	100	27.4	[112]
CPAM/Ti <sub>3</sub> C <sub>2</sub> T <sub>x</sub> MXene composite	NH <sub>3</sub>	100	25	[116]
Ti <sub>3</sub> C <sub>2</sub> T <sub>x</sub> MXene@TiO <sub>2</sub> /MoS <sub>2</sub> composite	NH <sub>3</sub>	100	164	[117]
Ti <sub>3</sub> C <sub>2</sub> T <sub>x</sub> MXene/rGO/SnO <sub>2</sub> aerogel	HCHO	10	54.9	[120]
Ni(OH) <sub>2</sub> /Ti <sub>3</sub> C <sub>2</sub> T <sub>x</sub> composite	NH <sub>3</sub>	50	13	[122]
SnS <sub>2</sub> /Ti <sub>3</sub> C <sub>2</sub> T <sub>x</sub> MXene composite	Acetone	50	29.8	[124]

### 2.2.6. Doped/Decorated MXenes

Doping is a popular method for enhancing the gas-sensing properties of metal oxides [125]. Few studies on the doping of MXenes for gas-sensing applications have been reported. Generally, noble metals with catalytic activity are used for decoration on the sensing materials, and since they are much more expensive than other materials, fewer studies have been conducted using noble metal decoration on MXenes. Also, doped MXenes are less studied relative to composite-based MXenes for gas-sensing application due to the lower impact of doping on the gas response relative to heterojunctions. However, in future studies much more attention should be paid to doped and decorated MXenes for gas-sensing studies. Heteroatom additions to MXenes can go to lattice sites, functional group sites or become adsorbed on surfaces. In general, element doping effects are as follows: (i) generation of active species and increase in conductance; (ii) adjustment of the electronic structure by introduction of defects; (iii) changing of the surface nature and chemical bonds in MXene; (iv) adjustment of the surface chemical properties to increase catalytic performance [126]. In this regard, S atoms with high electronegativity can decrease the electron density of the Ti atom, leading to a higher binding energy than that of Ti-C bonds. In a relevant study, it was demonstrated that the S doping of Ti<sub>3</sub>C<sub>2</sub>T<sub>x</sub> MXene led to a higher gas-sensing response to toluene than that of the pristine sensor. An enhanced response of 214% ((( $R_g - R_a$ ) /  $R_a$ ) × 100) to 1 ppm toluene was obtained after sulfur doping. Expansion of the interlayer spacing after sulfur doping has been reported; therefore, a larger surface area resulted in effective gas diffusion and provided more sites for toluene gas. Furthermore, the S at the surface of the MXenes acted like oxygen ions, leading to the expansion of the electron depletion layer (EDL) on the MXene. Upon interaction of toluene gas with these adsorbed sulfur species, they react with sulfur ions, and the

liberated electrons increase the concentration of electrons, leading to the appearance of a sensor signal. Moreover, owing to the donating effect of the ethyl group, a remarkable enhancement in the activity of the H<sub>2</sub> atoms on the benzene ring was observed, leading to enhanced selectivity for toluene gas. In addition, DFT calculations revealed an increase in the binding energy of toluene to the S-doped MXenes [127]. In another study, nitrogen-doped MXene (N-MXene) composited with poly 3, 4-ethylenedioxythio-phenol (PEDOT) and poly (4-styrenesulfonate) (PSS) (PEDOT:PSS) was used for sensing studies. The sensor with twice the amount of N-MXene relative to the polymer component exhibited a response of 25% ( $(|R_g - R_a|)/R_a \times 100$ ) to 25 ppm NH<sub>3</sub> gas at RT, which was higher than pristine counterparts. The doped N atoms with an electron-donor nature activated electron-transfer reactions and increased the number of sorption sites. Furthermore, the formation of n-p heterojunctions between the two components was ascribed to the sensing enhancement. In addition, the partial oxidation of MXene led to the formation of some TiO<sub>2</sub> NPs, which not only widened the interlayer spacing of MXene but also limited the restacking of the MXene layer [128].

A Au-decorated  $\alpha$ -Fe<sub>2</sub>O<sub>3</sub>/Ti<sub>3</sub>C<sub>2</sub>T<sub>x</sub> MXene nanocomposite disclosed a response of 16.9% ( $(|R_g - R_a|)/R_a \times 100$ ) to 1 ppm NH<sub>3</sub> gas at RT, with fast  $t_{res}$  and  $t_{rec}$  of 3 and 2 s, respectively. The surface area  $\alpha$ -Fe<sub>2</sub>O<sub>3</sub>/Ti<sub>3</sub>C<sub>2</sub>T<sub>x</sub> MXene nanocomposite was 57.34 m<sup>2</sup>/g, which provided sufficient adsorption sites for the NH<sub>3</sub> gas molecules. In addition, the presence of surface groups on MXene and the formation of heterojunctions between MXene/Fe<sub>2</sub>O<sub>3</sub> and Au/MXene and Au/Fe<sub>2</sub>O<sub>3</sub> contributed to the sensing signal. Moreover, Au, which has a good catalytic activity, has a promising effect on the adsorption and dissociation of oxygen and NH<sub>3</sub> gases from the surface of gas sensors. Based on DFT studies, the adsorption energy of NH<sub>3</sub> on nanocomposites (−8.31 eV) was much larger than that of other gases, reflecting the good selectivity of the sensor to NH<sub>3</sub> gas [129].

The Au-In<sub>2</sub>O<sub>3</sub>/Ti<sub>3</sub>C<sub>2</sub>T<sub>x</sub> MXene composite was prepared by a chemical synthesis route, followed by electrostatic self-assembly. The sensor exhibited a response of 31% ( $(|R_g - R_a|)/R_a \times 100$ ) to 5 ppm HCHO at RT. Moreover,  $t_{res}$  and  $t_{rec}$  were extremely rapid (5/4 s). The enhanced sensing properties were related to the catalytic effect of the Au NPs, the formation of heterojunctions between different components (Figure 18a), and the high surface area (27.75 m<sup>2</sup>/g) of the composite. Due to differences between the work functions of Au, In<sub>2</sub>O<sub>3</sub> and Ti<sub>3</sub>C<sub>2</sub>T<sub>x</sub> and in intimate contact, the electrons move from In<sub>2</sub>O<sub>3</sub> to Au, forming Schottky barriers in interfaces between In<sub>2</sub>O<sub>3</sub> and Au. Also, in interfaces between In<sub>2</sub>O<sub>3</sub> and Ti<sub>3</sub>C<sub>2</sub>T<sub>x</sub>, electrons move from In<sub>2</sub>O<sub>3</sub> to Ti<sub>3</sub>C<sub>2</sub>T<sub>x</sub> to equate the Fermi levels. Accordingly, in air, both Schottky barriers and heterojunction barriers form in interfaces. In a HCHO atmosphere, upon reaction of HCHO with adsorbed oxygen, the electrons return to the sensor surface and the heights of barriers change. This finally led to modulation of the electrical resistance in the HCHO environment. In addition, based on the DFT calculations, the adsorption energy of HCHO on the Au-In<sub>2</sub>O<sub>3</sub>/Ti<sub>3</sub>C<sub>2</sub>T<sub>x</sub> MXene composite was higher than that of the other sensors, confirming the high performance of the composite sensor for HCHO gas from an energy perspective (Figure 18b–d) [130].

Table 3 presents the RT gas-sensing properties of doped or decorated MXene-based gas sensors. They are mostly used for detection of NH<sub>3</sub>, C<sub>7</sub>H<sub>8</sub>, and HCHO gases at RT.

**Table 3.** RT gas-sensing properties of doped or decorated MXene-based gas sensors.

Sensing Material	Gas	Conc. (ppm)	Response (%) ( $( R_g - R_a )/R_a \times 100$ )	Ref.
S-doped Ti <sub>3</sub> C <sub>2</sub> T <sub>x</sub> MXene	C <sub>7</sub> H <sub>8</sub>	1	214	[127]
N-doped Ti <sub>3</sub> C <sub>2</sub> T <sub>x</sub> MXene-PEDOT:PSS	NH <sub>3</sub>	25	25	[128]
Au-decorated $\alpha$ -Fe <sub>2</sub> O <sub>3</sub> /Ti <sub>3</sub> C <sub>2</sub> T <sub>x</sub> MXene	NH <sub>3</sub>	1	16.9	[129]
Au-decorated In <sub>2</sub> O <sub>3</sub> /Ti <sub>3</sub> C <sub>2</sub> T <sub>x</sub> MXene composite	HCHO	5	31	[130]

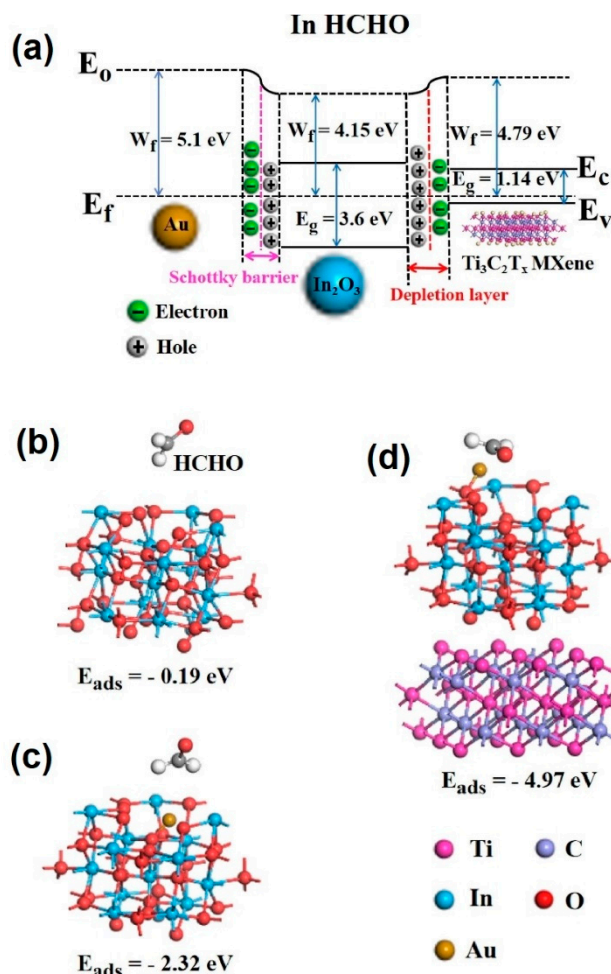


**Figure 18.** (a) The energy bands of Au-In<sub>2</sub>O<sub>3</sub>/Ti<sub>3</sub>C<sub>2</sub>T<sub>x</sub> MXene in HCHO. The optimized structure for HCHO adsorption system of (b) initial In<sub>2</sub>O<sub>3</sub>, (c) Au-In<sub>2</sub>O<sub>3</sub> and (d) Au-In<sub>2</sub>O<sub>3</sub>/Ti<sub>3</sub>C<sub>2</sub>T<sub>x</sub> MXene composite [116]. With permission from Elsevier.

### 3. Conclusions and Outlooks

In this review, we have discussed the RT gas-sensing properties of MXene-based gas sensors. Pristine MXene gas sensors without any modification often exhibit poor performance; hence, their surfaces can be modified to increase the number of surface functional groups or add new functional groups. Therefore, the response and selectivity can be increased. Composite fabrication with other materials, such as metal oxides, TMDs, and CPs, is a very popular and promising strategy for enhancing the RT performance of gas sensors. In particular, because of the highly intrinsic sensing properties of metal oxides, their composites with MXenes have led to the realization of high-performance gas sensors that can work at RT. Composites based on MXenes-TMDs have high surface areas and abundant surface groups, both of which are beneficial for gas sensing. Furthermore, composites with CPs are highly sensitive to NH<sub>3</sub> because of the high intrinsic sensitivities of both MXenes and CPs to this gas. Compared to MXene composites, less attention has been paid to doped MXenes, and more studies are needed in the future. Ternary composites are also promising for sensing applications; however, the optimization of all components is often difficult, and in this regard, more detailed studies are needed. In addition, the use of UV light to promote surface reactions and increase the number of active surface sites is a promising technique for enhancing the RT-sensing properties of MXene-based gas sensors.

From a performance point of view, generally, pristine MXene gas sensors suffer from low sensitivity, relatively poor selectivity and long  $t_{res}$  and  $t_{rec}$ , while doped and decorated MXene gas sensors show higher sensitivity, better selectivity and shorter dynamics. Also,

composite MXene-based gas sensors, especially those with metal oxides, exhibit the highest sensitivity, good selectivity and the shortest  $t_{res}$  and  $t_{rec}$ .

Thus, RT MXene-based gas sensors can be used to fabricate flexible gas sensors for wearable applications. However, since they must work at RT, where the humidity is generally high, their sensing properties should be less affected by the presence of humidity. Thus, surface treatment is a good strategy to decrease the hydrophilicity of MXenes. Decoration with noble metals such as Au, Pt, and Pd can be a good strategy for enhancing the selectivity of MXene-based gas sensors towards different gases, which requires further exploration.

**Author Contributions:** A.M.: writing and editing; M.H.L., H.S. and T.-U.K.: writing assistance; J.-Y.K.: editing assistance; S.S.K.: writing and review; H.W.K.: writing and review. All authors have read and agreed to the published version of the manuscript.

**Funding:** This study was supported by the Korea Polar Research Institute (KOPRI) grant funded by the Ministry of Oceans and Fisheries (KOPRI project No. PE22900), and the National Research Foundation of Korea (NRF) grant funded by the Korean government (MSIT) [2021R1A2C1009790]. In addition, this research was supported by Basic Science Research Program through the National Research Foundation of Korea (NRF) funded by the Ministry of Education (2016R1A6A1A03013422).

**Institutional Review Board Statement:** Not applicable.

**Informed Consent Statement:** Not applicable.

**Data Availability Statement:** These data can be found only in this article.

**Conflicts of Interest:** The authors declare no conflict of interest.

## References

1. Mirzaei, A.; Lee, J.H.; Majhi, S.M.; Weber, M.; Bechelany, M.; Kim, H.W.; Kim, S.S. Resistive gas sensors based on metal-oxide nanowires. *J. Appl. Phys.* **2019**, *126*, 241102. [[CrossRef](#)]
2. Mirzaei, A.; Neri, G. Microwave-assisted synthesis of metal oxide nanostructures for gas sensing application: A review. *Sens. Actuators B Chem.* **2016**, *237*, 749–775. [[CrossRef](#)]
3. Shooshtari, M.; Vollebregt, S.; Vaseghi, Y.; Rajati, M.; Pahlavan, S. The sensitivity enhancement of TiO<sub>2</sub>-based VOCs sensor decorated by gold at room temperature. *Nanotechnology* **2023**, *34*, 255501. [[CrossRef](#)]
4. Joshi, N.; Hayasaka, T.; Liu, Y.; Liu, H.; Oliveira, O.N.; Lin, L. A review on chemiresistive room temperature gas sensors based on metal oxide nanostructures, graphene and 2D transition metal dichalcogenides. *Mikrochim. Acta* **2018**, *185*, 213. [[CrossRef](#)]
5. Jiang, Q.; Lei, Y.; Liang, H.; Xi, K.; Xia, C.; Alshareef, H.N. Review of MXene electrochemical microsupercapacitors. *Energy Storage Mater.* **2020**, *27*, 78–95. [[CrossRef](#)]
6. Sreenilayam, S.P.; Ahad, I.U.; Nicolosi, V.; Brabazon, D. MXene materials based printed flexible devices for healthcare, biomedical and energy storage applications. *Mater. Today* **2021**, *43*, 99–131.
7. Ma, C.; Ma, M.G.; Si, C.; Ji, X.X.; Wan, P. Flexible MXene-based composites for wearable devices. *Adv. Fun. Mater.* **2021**, *31*, 2009524. [[CrossRef](#)]
8. Li, X.; Huang, Z.; Shuck, C.E.; Liang, G.; Gogotsi, Y.; Zhi, C. MXene chemistry, electrochemistry and energy storage applications. *Nat. Rev. Chem.* **2022**, *6*, 389–404. [[CrossRef](#)]
9. Bhat, A.; Anwer, S.; Bhat, K.S.; Mohideen, M.I.H.; Liao, K.; Qurashi, A. Prospects challenges and stability of 2D MXenes for clean energy conversion and storage applications. *NPJ 2D Mater. Appl.* **2021**, *5*, 61. [[CrossRef](#)]
10. Murali, G.; Reddy Modigunta, J.K.; Park, Y.H.; Lee, J.H.; Rawal, J.; Lee, S.Y.; In, I.; Park, S.J. A review on MXene synthesis, stability, and photocatalytic applications. *ACS Nano* **2022**, *16*, 13370–13429. [[CrossRef](#)]
11. Murali, G.; Reddy Modigunta, J.K.; Park, Y.H.; Lee, J.H.; Lee, S.Y.; Park, S.J.; In, I. A review on MXenes: New-generation 2D materials for supercapacitors. *Sustain. Energy Fuels* **2021**, *5*, 5672–5693.
12. Bhardwaj, R.; Hazra, A. MXene-based gas sensors. *J. Mater. Chem. C* **2021**, *9*, 15735–15754. [[CrossRef](#)]
13. Mehdi Aghaei, S.; Aasi, A.; Panchapakesan, B. Experimental and theoretical advances in MXene-based gas sensors. *ACS Omega* **2021**, *6*, 2450–2461. [[CrossRef](#)] [[PubMed](#)]
14. Zhang, H.F.; Xuan, J.Y.; Zhang, Q.; Sun, M.L.; Jia, F.C.; Wang, X.M.; Yin, G.C.; Lu, S.Y. Strategies and challenges for enhancing performance of MXene-based gas sensors: A review. *Rare Met.* **2022**, *41*, 3976–3999. [[CrossRef](#)]
15. Devaraj, M.; Rajendran, S.; Hoang, T.K.; Soto-Moscoso, M. A review on MXene and its nanocomposites for the detection of toxic inorganic gases. *Chemosphere* **2022**, *302*, 134933. [[CrossRef](#)]
16. Xia, Q.; Fan, Y.; Li, S.; Zhou, A.; Shinde, N.; Mane, R.S. MXene-based chemical gas sensors: Recent developments and challenges. *Diam. Relat. Mater.* **2022**, *131*, 109557. [[CrossRef](#)]
17. Nahirniak, S.; Saruhan, B. MXene heterostructures as perspective materials for gas sensing applications. *Sensors* **2022**, *22*, 972. [[CrossRef](#)]

18. Riazi, H.; Taghizadeh, G.; Soroush, M. MXene-based nanocomposite sensors. *ACS Omega* **2021**, *6*, 11103–11112. [[CrossRef](#)]
19. Pei, Y.; Zhang, X.; Hui, Z.; Zhou, J.; Huang, X.; Sun, G.; Huang, W.  $\text{Ti}_3\text{C}_2\text{T}_x$  MXene for sensing applications: Recent progress, design principles, and future perspectives. *ACS Nano* **2021**, *15*, 3996–4017. [[CrossRef](#)]
20. Deshmukh, K.; Kovářik, T.; Pasha, S.K. State of the art recent progress in two dimensional MXenes based gas sensors and biosensors: A comprehensive review. *Coord. Chem. Rev.* **2020**, *424*, 213514.
21. Sinha, A.; Zhao, H.; Huang, Y.; Lu, X.; Chen, J.; Jain, R. MXene: An emerging material for sensing and biosensing. *TrAC Tren. Anal. Chem.* **2018**, *105*, 424–435.
22. Otgonbayar, Z.; Oh, W.C. Comprehensive and multi-functional MXene based sensors: An updated review. *FlatChem* **2023**, *40*, 100524.
23. Ta, Q.T.H.; Thakur, D.; Noh, J.S. Design of functional  $\text{Ti}_3\text{C}_2\text{T}_x$  MXene for gas sensors and energy harvesting: A review. *Chemosensors* **2023**, *11*, 477.
24. Jin, C.; Bai, Z. MXene-based textile sensors for wearable applications. *ACS Sens.* **2022**, *7*, 929–950. [[CrossRef](#)] [[PubMed](#)]
25. Radhakrishnan, S.; Rout, C.S. Recent developments in 2D MXene based materials for next generation room temperature  $\text{NO}_2$  gas sensors. *Nanoscale Adv.* **2023**, *5*, 4649–4669.
26. Peng, B.; Huang, X. Research status of gas sensing performance of  $\text{Ti}_3\text{C}_2\text{T}_x$ -based gas sensors: A mini review. *Fron. Chem.* **2022**, *10*, 1037732. [[CrossRef](#)]
27. Gautam, R.; Marriwala, N.; Devi, R. A review: Study of MXene and graphene together. *Meas. Sens.* **2022**, *25*, 100592. [[CrossRef](#)]
28. Lee, E.; Kim, D.J. Recent exploration of two-dimensional MXenes for gas sensing: From a theoretical to an experimental view. *J. Electrochem. Soc.* **2020**, *167*, 037515. [[CrossRef](#)]
29. Xin, M.; Li, J.; Ma, Z.; Pan, L.; Shi, Y. MXenes and their applications in wearable sensors. *Front. Chem.* **2020**, *8*, 297. [[CrossRef](#)]
30. Sivasankarapillai, V.S.; Sharma, T.S.K.; Hwa, K.Y.; Wabaidur, S.M.; Angaiah, S.; Dhanusuraman, R. MXene based sensing materials: Current status and future perspectives. *ES Energy Environ.* **2022**, *15*, 4–14. [[CrossRef](#)]
31. Simonenko, E.P.; Simonenko, N.P.; Mokrushin, A.S.; Simonenko, T.L.; Gorobtsov, P.Y.; Nagornov, I.A.; Korotcenkov, G.; Sysoev, V.V.; Kuznetsov, N.T. Application of titanium carbide MXenes in chemiresistive gas sensors. *Nanomaterials* **2023**, *13*, 850.
32. Tran, V.A.; Tran, N.T.; Doan, V.D.; Nguyen, T.Q.; Thi, H.H.P.; Vo, G.N. Application prospects of MXenes materials modifications for sensors. *Micromachines* **2023**, *14*, 247. [[CrossRef](#)]
33. Li, Q.; Li, Y.; Zeng, W. Preparation and application of 2D MXene-based gas sensors: A review. *Chemosensors* **2021**, *9*, 225. [[CrossRef](#)]
34. Naguib, M.; Kurtoglu, M.; Presser, V.; Lu, J.; Niu, J.; Heon, M.; Hultman, L.; Gogotsi, Y.; Barsoum, M.W. Two-dimensional nanocrystals produced by exfoliation of  $\text{Ti}_3\text{AlC}_2$ . *Adv. Mater.* **2011**, *23*, 4248–4253. [[CrossRef](#)]
35. Gogotsi, Y.; Anasori, B. The rise of MXenes. *ACS Nano* **2019**, *13*, 8491–8494. [[CrossRef](#)] [[PubMed](#)]
36. Lamiel, C.; Hussain, I.; Warner, J.H.; Zhang, K. Beyond Ti-based MXenes: A review of emerging non-Ti based metal-MXene structure, properties, and applications. *Mater. Today* **2023**, *63*, 313–338. [[CrossRef](#)]
37. Huang, Y.; Lu, Q.; Wu, D.; Jiang, Y.; Liu, Z.; Chen, B.; Zhu, M.; Schmidt, O.G. Flexible MXene films for batteries and beyond. *Carbon Energy* **2022**, *4*, 598–620. [[CrossRef](#)]
38. Salim, O.; Mahmoud, K.A.; Pant, K.K.; Joshi, R.K. Introduction to MXenes: Synthesis and characteristics. *Mater. Today Chem.* **2019**, *14*, 100191. [[CrossRef](#)]
39. Bashir, T.; Ismail, S.A.; Wang, J.; Zhu, W.; Zhao, J.; Gao, L. MXene terminating groups O,–F or –OH,–F or O,–OH,–F, or O,–OH,–Cl? *J. Energy Chem.* **2023**, *76*, 90–104. [[CrossRef](#)]
40. Kumar, J.A.; Prakash, P.; Krithiga, T.; Amarnath, D.J.; Premkumar, J.; Rajamohan, N.; Vasseghian, Y.; Saravanan, P.; Rajasimman, M. Methods of synthesis, characteristics, and environmental applications of MXene: A comprehensive review. *Chemosphere* **2022**, *286*, 131607. [[CrossRef](#)]
41. Lim, K.R.G.; Shekhirev, M.; Wyatt, B.C.; Anasori, B.; Gogotsi, Y.; Seh, Z.W. Fundamentals of MXene synthesis. *Nat. Synth* **2022**, *1*, 601–614. [[CrossRef](#)]
42. VahidMohammadi, A.; Rosen, J.; Gogotsi, Y. The world of two-dimensional carbides and nitrides (MXenes). *Science* **2021**, *372*, 1581. [[CrossRef](#)]
43. Naguib, M.; Barsoum, M.W.; Gogotsi, Y. Ten years of progress in the synthesis and development of MXenes. *Adv. Mater.* **2021**, *33*, 2103393. [[CrossRef](#)]
44. Ullah, S.; Shahzad, F.; Qiu, B.; Fang, X.; Ammar, A.; Luo, Z.; Zaidi, S.A. MXene-based aptasensors: Advances, challenges, and prospects. *Prog. Mater. Sci.* **2022**, *129*, 100967.
45. Jin, S.; Guo, Y.; Wang, F.; Zhou, A. The synthesis of MXenes. *MRS Bull.* **2023**, *48*, 245–252.
46. Chen, T.; Yan, W.; Wang, Y.; Li, J.; Hu, H.; Ho, D.  $\text{SnS}_2/\text{MXene}$  derived  $\text{TiO}_2$  hybrid for ultra-fast room temperature  $\text{NO}_2$  gas sensing. *J. Mater. Chem. C* **2021**, *9*, 7407–7416. [[CrossRef](#)]
47. Zhang, B.; Li, Z.; Li, C.; Li, M.; Fu, C.; Tao, R.; Zha, X.H.; Li, H.; Luo, J. High-sensitive ppb-level ammonia QCM sensor based on sulfur doped  $\text{Ti}_3\text{C}_2\text{T}_x$  MXene. *Sens. Actuator A Phys.* **2023**, *350*, 114138. [[CrossRef](#)]
48. Ta, Q.T.H.; Thakur, D.; Noh, J.S. Enhanced Gas Sensing Performance of  $\text{ZnO}/\text{Ti}_3\text{C}_2\text{T}_x$  MXene Nanocomposite. *Micromachines* **2022**, *13*, 1710. [[CrossRef](#)]
49. Huang, K.; Li, C.; Li, H.; Ren, G.; Wang, L.; Wang, W.; Meng, X. Photocatalytic applications of two-dimensional  $\text{Ti}_3\text{C}_2$  MXenes: A review. *ACS Appl. Nano Mater.* **2020**, *3*, 9581–9603. [[CrossRef](#)]

50. Adomavičiūtė-Grabusovė, S.; Ramanavičius, S.; Popov, A.; Šablinskas, V.; Gogotsi, O.; Ramanavičius, A. Selective enhancement of SERS spectral bands of salicylic acid adsorbate on 2D  $\text{Ti}_3\text{C}_2\text{T}_x$ -based MXene film. *Chemosensors* **2021**, *9*, 223. [[CrossRef](#)]
51. Lee, E.; VahidMohammadi, A.; Prorok, B.C.; Yoon, Y.S.; Beidaghi, M.; Kim, D.J. Room temperature gas sensing of two-dimensional titanium carbide (MXene). *ACS Appl. Mater. Interfaces* **2017**, *9*, 37184–37190. [[CrossRef](#)]
52. Ansari, H.R.; Mirzaei, A.; Shokrollahi, H.; Kumar, R.; Kim, J.Y.; Kim, H.W.; Kumar, M.; Kim, S.S. Flexible/wearable resistive gas sensors based on 2D materials. *J. Mater. Chem. C* **2023**, *11*, 6528–6549. [[CrossRef](#)]
53. Bag, A.; Lee, N.E. Recent advancements in development of wearable gas sensors. *Adv. Mater. Technol.* **2021**, *6*, 2000883. [[CrossRef](#)]
54. Kim, S.J.; Koh, H.J.; Ren, C.E.; Kwon, O.; Maleski, K.; Cho, S.Y.; Anasori, B.; Kim, C.K.; Choi, Y.K.; Kim, J.; et al. Metallic  $\text{Ti}_3\text{C}_2\text{T}_x$  MXene gas sensors with ultrahigh signal-to-noise ratio. *ACS Nano* **2018**, *12*, 986–993. [[CrossRef](#)] [[PubMed](#)]
55. Liu, F.; Zhou, A.; Chen, J.; Jia, J.; Zhou, W.; Wang, L.; Hu, Q. Preparation of  $\text{Ti}_3\text{C}_2$  and  $\text{Ti}_2\text{C}$  MXenes by fluoride salts etching and methane adsorptive properties. *Appl. Surf. Sci.* **2017**, *416*, 781–789. [[CrossRef](#)]
56. Wu, M.; He, M.; Hu, Q.; Wu, Q.; Sun, G.; Xie, L.; Zhang, Z.; Zhu, Z.; Zhou, A.  $\text{Ti}_3\text{C}_2$  MXene-based sensors with high selectivity for  $\text{NH}_3$  detection at room temperature. *ACS Sens.* **2019**, *4*, 2763–2770. [[CrossRef](#)]
57. Wang, Y.; Fu, J.; Xu, J.; Hu, H.; Ho, D. Atomic Plasma Grafting: Precise Control of Functional Groups on  $\text{Ti}_3\text{C}_2\text{T}_x$  MXene for Room Temperature Gas Sensors. *ACS Appl. Mater. Interfaces* **2023**, *15*, 12232–12239. [[CrossRef](#)]
58. Kim, H.; Wang, Z.; Alshareef, H.N. MXetronics: Electronic and photonic applications of MXenes. *Nano Energy* **2019**, *60*, 179–197. [[CrossRef](#)]
59. Li, X.; An, Z.; Lu, Y.; Shan, J.; Xing, H.; Liu, G.; Shi, Z.; He, Y.; Chen, Q.; Han, R.P.; et al. Room Temperature VOCs Sensing with Termination-Modified  $\text{Ti}_3\text{C}_2\text{T}_x$  MXene for Wearable Exhaled Breath Monitoring. *Adv. Mater. Technol.* **2022**, *7*, 2100872. [[CrossRef](#)]
60. Kumar, A.N.; Pal, K. Amine-functionalized stable  $\text{Nb}_2\text{CT}_x$  MXene toward room temperature ultrasensitive  $\text{NO}_2$  gas sensor. *Mater. Adv.* **2022**, *3*, 5151–5162. [[CrossRef](#)]
61. Koh, H.J.; Kim, S.J.; Maleski, K.; Cho, S.Y.; Kim, Y.J.; Ahn, C.W.; Gogotsi, Y.; Jung, H.T. Enhanced selectivity of MXene gas sensors through metal ion intercalation: In situ X-ray diffraction study. *ACS Sens.* **2019**, *4*, 1365–1372. [[CrossRef](#)]
62. Zhang, Y.; Jiang, Y.; Duan, Z.; Huang, Q.; Wu, Y.; Liu, B.; Zhao, Q.; Wang, S.; Yuan, Z.; Tai, H. Highly sensitive and selective  $\text{NO}_2$  sensor of alkalinized  $\text{V}_2\text{CT}_x$  MXene driven by interlayer swelling. *Sens. Actuators B Chem.* **2021**, *344*, 130150. [[CrossRef](#)]
63. Yang, Z.; Liu, A.; Wang, C.; Liu, F.; He, J.; Li, S.; Wang, J.; You, R.; Yan, X.; Sun, P.; et al. Improvement of gas and humidity sensing properties of organ-like MXene by alkaline treatment. *ACS Sens.* **2019**, *4*, 1261–1269. [[CrossRef](#)] [[PubMed](#)]
64. Lee, E.; VahidMohammadi, A.; Yoon, Y.S.; Beidaghi, M.; Kim, D.J. Two-dimensional vanadium carbide MXene for gas sensors with ultrahigh sensitivity toward nonpolar gases. *ACS Sens.* **2019**, *4*, 1603–1611. [[CrossRef](#)] [[PubMed](#)]
65. Majhi, S.M.; Ali, A.; Greish, Y.E.; El-Maghraby, H.F.; Qamhieh, N.N.; Hajamohideen, A.R.; Mahmoud, S.T. Accordion-like- $\text{Ti}_3\text{C}_2$  MXene-based gas sensors with sub-ppm level detection of acetone at room temperature. *ACS Appl. Electron. Mater.* **2022**, *4*, 4094–4103. [[CrossRef](#)]
66. Thomas, T.; Ramon, J.A.R.; Agarwal, V.; Álvarez-Méndez, A.; Martínez, J.A.; Kumar, Y.; Sanal, K.C. Highly stable, fast responsive  $\text{Mo}_2\text{CT}_x$  MXene sensors for room temperature carbon dioxide detection. *Microporous Mesoporous Mater.* **2022**, *336*, 11. [[CrossRef](#)]
67. Guo, W.; Surya, S.G.; Babar, V.; Ming, F.; Sharma, S.; Alshareef, H.N.; Schwingenschlogl, U.; Salama, K.N. Selective toluene detection with  $\text{Mo}_2\text{CT}_x$  MXene at room temperature. *ACS Appl. Mater. Interfaces* **2020**, *12*, 57218–57227. [[CrossRef](#)]
68. Lam, K.C.; Huang, B.; Shi, S.Q. Room-temperature methane gas sensing properties based on in situ reduced graphene oxide incorporated with tin dioxide. *J. Mater. Chem. A* **2017**, *5*, 11131–11142. [[CrossRef](#)]
69. Wang, J.; Xu, R.; Xia, Y.; Komarneni, S.  $\text{Ti}_2\text{CT}_x$  MXene: A novel p-type sensing material for visible light-enhanced room temperature methane detection. *Ceram. Int.* **2021**, *47*, 34437–34442. [[CrossRef](#)]
70. Sun, S.; Wang, M.; Chang, X.; Jiang, Y.; Zhang, D.; Wang, D.; Zhang, Y.; Lei, Y.  $\text{W}_{18}\text{O}_{49}/\text{Ti}_3\text{C}_2\text{T}_x$  MXene nanocomposites for highly sensitive acetone gas sensor with low detection limit. *Sens. Actuators B Chem.* **2020**, *304*, 127274. [[CrossRef](#)]
71. Zhou, J.; Hosseini Shokouh, S.H.; Komsa, H.P.; Rieppo, L.; Cui, L.; Lv, Z.P.; Kordas, K. MXene-Polymer Hybrid for High-Performance Gas Sensor Prepared by Microwave-Assisted In-Situ Intercalation. *Adv. Mater. Technol.* **2022**, *7*, 2101565. [[CrossRef](#)]
72. Zhu, Y.; Ma, Y.; Wu, D.; Jiang, G. Preparation and gas sensing properties of  $\text{ZnO}/\text{MXene}$  composite nanomaterials. *Sens. Actuator A Phys.* **2022**, *344*, 113740. [[CrossRef](#)]
73. Niu, G.; Zhang, M.; Wu, B.; Zhuang, Y.; Ramachandran, R.; Zhao, C.; Wang, F. Nanocomposites of pre-oxidized  $\text{Ti}_3\text{C}_2\text{T}_x$  MXene and  $\text{SnO}_2$  nanosheets for highly sensitive and stable formaldehyde gas sensor. *Ceram. Int.* **2023**, *49*, 2583–2590. [[CrossRef](#)]
74. Zhan, X.; Si, C.; Zhou, J.; Sun, Z. MXene and MXene-based composites: Synthesis, properties and environment-related applications. *Nanoscale Horiz.* **2020**, *5*, 235–258. [[CrossRef](#)]
75. He, T.; Liu, W.; Lv, T.; Ma, M.; Liu, Z.; Vasiliev, A.; Li, X. MXene/ $\text{SnO}_2$  heterojunction based chemical gas sensors. *Sens. Actuators B Chem.* **2021**, *329*, 129275. [[CrossRef](#)]
76. Gasso, S.; Sohal, M.K.; Mahajan, A. MXene modulated  $\text{SnO}_2$  gas sensor for ultra-responsive room-temperature detection of  $\text{NO}_2$ . *Sens. Actuators B Chem.* **2022**, *357*, 131427. [[CrossRef](#)]
77. Yao, L.; Tian, X.; Cui, X.; Zhao, R.; Xiao, M.; Wang, B.; Xiao, X.; Wang, Y. Two-dimensional  $\text{Ti}_3\text{C}_2\text{T}_x$  MXene/ $\text{SnO}$  nanocomposites: Towards enhanced response and selective ammonia vapor sensor at room temperature. *Sens. Actuators B Chem.* **2022**, *358*, 131501. [[CrossRef](#)]
78. Yu, H.; Dai, L.; Liu, Y.; Zhou, Y.; Fan, P.; Luo, J.; Zhong, A.  $\text{Ti}_3\text{C}_2\text{T}_x$  MXene- $\text{SnO}_2$  nanocomposite for superior room temperature ammonia gas sensor. *J. Alloys Compd.* **2023**, *962*, 171170. [[CrossRef](#)]

79. Yang, J.; Gui, Y.; Wang, Y.; He, S. NiO/Ti<sub>3</sub>C<sub>2</sub>T<sub>x</sub> MXene nanocomposites sensor for ammonia gas detection at room temperature. *J. Ind. Eng. Chem.* **2023**, *119*, 476–484. [[CrossRef](#)]
80. Huang, B.; Tong, X.; Zhang, X.; Feng, Q.; Rumyantseva, M.N.; Prakash, J.; Li, X. MXene/NiO Composites for Chemiresistive-Type Room Temperature Formaldehyde Sensor. *Chemosensors* **2023**, *11*, 258. [[CrossRef](#)]
81. Liu, Z.; He, T.; Sun, H.; Huang, B.; Li, X. Layered MXene heterostructured with In<sub>2</sub>O<sub>3</sub> nanoparticles for ammonia sensors at room temperature. *Sens. Actuators B Chem.* **2022**, *365*, 131918. [[CrossRef](#)]
82. He, T.; Sun, S.; Huang, B.; Li, X. MXene/SnS<sub>2</sub> Heterojunction for Detecting Sub-ppm NH<sub>3</sub> at Room Temperature. *ACS Appl. Mater. Interfaces* **2023**, *15*, 4194–4207. [[CrossRef](#)] [[PubMed](#)]
83. Liu, M.; Wang, Z.; Song, P.; Yang, Z.; Wang, Q. In<sub>2</sub>O<sub>3</sub> nanocubes/Ti<sub>3</sub>C<sub>2</sub>T<sub>x</sub> MXene composites for enhanced methanol gas sensing properties at room temperature. *Ceram. Int.* **2021**, *47*, 23028–23037. [[CrossRef](#)]
84. Liu, M.; Wang, J.; Song, P.; Ji, J.; Wang, Q. Metal-organic frameworks-derived In<sub>2</sub>O<sub>3</sub> microtubes/Ti<sub>3</sub>C<sub>2</sub>T<sub>x</sub> MXene composites for NH<sub>3</sub> detection at room temperature. *Sens. Actuators B Chem.* **2022**, *361*, 131755. [[CrossRef](#)]
85. Liu, M.; Ji, J.; Song, P.; Liu, M.; Wang, Q. α-Fe<sub>2</sub>O<sub>3</sub> nanocubes/Ti<sub>3</sub>C<sub>2</sub>T<sub>x</sub> MXene composites for improvement of acetone sensing performance at room temperature. *Sens. Actuators B Chem.* **2021**, *349*, 130782. [[CrossRef](#)]
86. Liu, M.; Ji, J.; Song, P.; Wang, J.; Wang, Q. Sensing performance of α-Fe<sub>2</sub>O<sub>3</sub>/Ti<sub>3</sub>C<sub>2</sub>T<sub>x</sub> MXene nanocomposites to NH<sub>3</sub> at room temperature. *J. Alloys Compd.* **2022**, *898*, 162812. [[CrossRef](#)]
87. Gasso, S.; Mahajan, A. MXene decorated tungsten trioxide nanocomposite-based sensor capable of detecting NO<sub>2</sub> gas down to ppb-level at room temperature. *Mater. Sci. Semicond.* **2022**, *152*, 107048. [[CrossRef](#)]
88. Guo, X.; Ding, Y.; Kuang, D.; Wu, Z.; Sun, X.; Du, B.; Liang, C.; Wu, Y.; Qu, W.; Xiong, L.; et al. Enhanced ammonia sensing performance based on MXene-Ti<sub>3</sub>C<sub>2</sub>T<sub>x</sub> multilayer nanoflakes functionalized by tungsten trioxide nanoparticles. *J. Colloid Interface Sci.* **2021**, *595*, 6–14. [[CrossRef](#)]
89. Liu, M.; Ding, Y.; Lu, Z.; Song, P.; Wang, Q. Layered Ti<sub>3</sub>C<sub>2</sub>T<sub>x</sub> MXene/CuO spindles composites for NH<sub>3</sub> detection at room-temperature. *J. Alloys Compd.* **2023**, *938*, 168563. [[CrossRef](#)]
90. Guo, F.; Feng, C.; Zhang, Z.; Zhang, L.; Xu, C.; Zhang, C.; Lin, S.; Wu, H.; Zhang, B.; Tabusi, A.; et al. A room-temperature NO<sub>2</sub> sensor based on Ti<sub>3</sub>C<sub>2</sub>T<sub>x</sub> MXene modified with sphere-like CuO. *Sens. Actuators B Chem.* **2023**, *375*, 132885. [[CrossRef](#)]
91. Mokrushin, A.S.; Nagornov, I.A.; Averin, A.A.; Simonenko, T.L.; Simonenko, N.P.; Simonenko, E.P.; Kuznetsov, N.T. Chemoresistive Properties of V<sub>2</sub>CT<sub>x</sub> MXene and the V<sub>2</sub>CT<sub>x</sub>/V<sub>3</sub>O<sub>7</sub> Nanocomposite Based on It. *Chemosensors* **2023**, *11*, 142. [[CrossRef](#)]
92. Majhi, S.M.; Ali, A.; Greish, Y.E.; El-Maghraby, H.F.; Mahmoud, S.T. V<sub>2</sub>CT<sub>x</sub> MXene-based hybrid sensor with high selectivity and ppb-level detection for acetone at room temperature. *Sci. Rep.* **2023**, *13*, 3114. [[CrossRef](#)] [[PubMed](#)]
93. Choi, J.; Kim, Y.J.; Cho, S.Y.; Park, K.; Kang, H.; Kim, S.J.; Jung, H.T. In situ formation of multiple schottky barriers in a Ti<sub>3</sub>C<sub>2</sub> MXene film and its application in highly sensitive gas sensors. *Adv. Funct. Mater.* **2020**, *30*, 2003998. [[CrossRef](#)]
94. Mokrushin, A.S.; Nagornov, I.A.; Gorobtsov, P.Y.; Averin, A.A.; Simonenko, T.L.; Simonenko, N.P.; Simonenko, E.P.; Kuznetsov, N.T. Effect of Ti<sub>2</sub>CT<sub>x</sub> MXene Oxidation on Its Gas-Sensitive Properties. *Chemosensors* **2022**, *11*, 13. [[CrossRef](#)]
95. Wang, J.; Yang, Y.; Xia, Y. Mesoporous MXene/ZnO nanorod hybrids of high surface area for UV-activated NO<sub>2</sub> gas sensing in ppb-level. *Sens. Actuators B Chem.* **2022**, *353*, 131087. [[CrossRef](#)]
96. Fan, C.; Shi, J.; Zhang, Y.; Quan, W.; Chen, X.; Yang, J.; Zeng, M.; Zhou, Z.; Su, Y.; Wei, H.; et al. Fast and recoverable NO<sub>2</sub> detection achieved by assembling ZnO on Ti<sub>3</sub>C<sub>2</sub>T<sub>x</sub> MXene nanosheets under UV illumination at room temperature. *Nanoscale* **2022**, *14*, 3441–3451. [[CrossRef](#)]
97. Zhang, D.; Yu, S.; Wang, X.; Huang, J.; Pan, W.; Zhang, J.; Meteku, B.E.; Zeng, J. UV illumination-enhanced ultrasensitive ammonia gas sensor based on (001) TiO<sub>2</sub>/MXene heterostructure for food spoilage detection. *J. Hazard. Mater.* **2022**, *423*, 127160. [[CrossRef](#)]
98. Sima, Z.; Song, P.; Ding, Y.; Lu, Z.; Wang, Q. ZnSnO<sub>3</sub> nanocubes/Ti<sub>3</sub>C<sub>2</sub>T<sub>x</sub> MXene composites for enhanced formaldehyde gas sensing properties at room temperature. *Appl. Surf. Sci.* **2022**, *598*, 153861. [[CrossRef](#)]
99. Zheng, W.; Liu, X.; Xie, J.; Lu, G.; Zhang, J. Emerging van der Waals junctions based on TMDs materials for advanced gas sensors. *Coord. Chem. Rev.* **2021**, *447*, 214151. [[CrossRef](#)]
100. Kumar, S.; Pavelyev, V.; Mishra, P.; Tripathi, N.; Sharma, P.; Calle, F. A review on 2D transition metal di-chalcogenides and metal oxide nanostructures based NO<sub>2</sub> gas sensors. *Mater. Sci. Semicond.* **2020**, *107*, 104865. [[CrossRef](#)]
101. Chen, W.Y.; Jiang, X.; Lai, S.N.; Peroulis, D.; Stanciu, L. Nanohybrids of a MXene and transition metal dichalcogenide for selective detection of volatile organic compounds. *Nat. Commun.* **2020**, *11*, 1302. [[CrossRef](#)] [[PubMed](#)]
102. Quan, W.; Shi, J.; Luo, H.; Fan, C.; Lv, W.; Chen, X.; Zeng, M.; Yang, J.; Hu, N.; Su, Y.; et al. Fully Flexible MXene-based Gas Sensor on Paper for Highly Sensitive Room-Temperature Nitrogen Dioxide Detection. *ACS Sens.* **2023**, *8*, 103–113. [[CrossRef](#)] [[PubMed](#)]
103. Ta, Q.T.H.; Tri, N.N.; Noh, J.S. Improved NO<sub>2</sub> gas sensing performance of 2D MoS<sub>2</sub>/Ti<sub>3</sub>C<sub>2</sub>T<sub>x</sub> MXene nanocomposite. *Appl. Surf. Sci.* **2022**, *604*, 154624. [[CrossRef](#)]
104. Yan, H.; Chu, L.; Li, Z.; Sun, C.; Shi, Y.; Ma, J. 2H-MoS<sub>2</sub>/Ti<sub>3</sub>C<sub>2</sub>T<sub>x</sub> MXene composites for enhanced NO<sub>2</sub> gas sensing properties at room temperature. *Sens. Actuators Rep.* **2022**, *4*, 100103. [[CrossRef](#)]
105. Xia, Y.; He, S.; Wang, J.; Zhou, L.; Wang, J.; Komarneni, S. MXene/WS<sub>2</sub> hybrids for visible-light-activated NO<sub>2</sub> sensing at room temperature. *ChemComm* **2021**, *57*, 9136–9139. [[CrossRef](#)]
106. Vasseghian, Y.; Doan, V.D.; Nguyen, T.T.T.; Vo, T.T.T.; Do, H.H.; Vu, K.B.; Vu, Q.H.; Dai Lam, T.; Tran, V.A. Flexible and high-sensitivity sensor based on Ti<sub>3</sub>C<sub>2</sub>-MoS<sub>2</sub> MXene composite for the detection of toxic gases. *Chemosphere* **2022**, *291*, 133025. [[CrossRef](#)]

107. Liu, X.; Zheng, W.; Kumar, R.; Kumar, M.; Zhang, J. Conducting polymer-based nanostructures for gas sensors. *Coord. Chem. Rev.* **2022**, *462*, 214517. [[CrossRef](#)]
108. Kumar, V.; Mirzaei, A.; Bonyani, M.; Kim, K.H.; Kim, H.W.; Kim, S.S. Advances in electrospun nanofiber fabrication for polyaniline (PANI)-based chemoresistive sensors for gaseous ammonia. *TrAC Trends Anal. Chem.* **2020**, *129*, 115938. [[CrossRef](#)]
109. Yan, Y.; Yang, G.; Xu, J.L.; Zhang, M.; Kuo, C.C.; Wang, S.D. Conducting polymer-inorganic nanocomposite-based gas sensors: A review. *STAM* **2020**, *21*, 768–786. [[CrossRef](#)]
110. Jin, L.; Wu, C.; Wei, K.; He, L.; Gao, H.; Zhang, H.; Zhang, K.; Asiri, A.M.; Alamry, K.A.; Yang, L.; et al. Polymeric Ti<sub>3</sub>C<sub>2</sub>T<sub>x</sub> MXene composites for room temperature ammonia sensing. *ACS Appl. Nano Mater.* **2020**, *3*, 12071–12079. [[CrossRef](#)]
111. Cai, Y.; Wang, Y.; Wen, X.; Xiong, J.; Song, H.; Li, Z.; Zu, D.; Shen, Y.; Li, C. Ti<sub>3</sub>C<sub>2</sub>T<sub>x</sub> MXene/urchin-like PANI hollow nanosphere composite for high performance flexible ammonia gas sensor. *Anal. Chim. Acta* **2022**, *1225*, 340256. [[CrossRef](#)] [[PubMed](#)]
112. Zhao, L.; Wang, K.; Wei, W.; Wang, L.; Han, W. High-performance flexible sensing devices based on polyaniline/MXene nanocomposites. *InfoMat* **2019**, *1*, 407–416. [[CrossRef](#)]
113. Hosseini-Shokouh, S.H.; Zhou, J.; Berger, E.; Lv, Z.P.; Hong, X.; Virtanen, V.; Kordas, K.; Komsa, H.P. Highly Selective H<sub>2</sub>S Gas Sensor Based on Ti<sub>3</sub>C<sub>2</sub>T<sub>x</sub> MXene–Organic Composites. *ACS Appl. Mater. Interfaces* **2023**, *15*, 7063–7073. [[CrossRef](#)] [[PubMed](#)]
114. Zhao, L.; Zheng, Y.; Wang, K.; Lv, C.; Wei, W.; Wang, L.; Han, W. Highly stable cross-linked cationic polyacrylamide/Ti<sub>3</sub>C<sub>2</sub>T<sub>x</sub> MXene nanocomposites for flexible ammonia-recognition devices. *Adv. Mater. Technol.* **2020**, *5*, 2000248. [[CrossRef](#)]
115. Wang, Z.; Wang, F.; Hermawan, A.; Asakura, Y.; Hasegawa, T.; Kumagai, H.; Kato, H.; Kakihana, M.; Zhu, J.; Yin, S. SnO-SnO<sub>2</sub> modified two-dimensional MXene Ti<sub>3</sub>C<sub>2</sub>T<sub>x</sub> for acetone gas sensor working at room temperature. *J. Mater. Sci. Technol.* **2021**, *73*, 128–138. [[CrossRef](#)]
116. Ranjbar, F.; Hajati, S.; Ghaedi, M.; Dashtian, K.; Naderi, H.; Toth, J. Highly selective MXene/V<sub>2</sub>O<sub>5</sub>/CuWO<sub>4</sub>-based ultra-sensitive room temperature ammonia sensor. *J. Hazard. Mater.* **2021**, *416*, 126196. [[CrossRef](#)]
117. Tian, X.; Yao, L.; Cui, X.; Zhao, R.; Chen, T.; Xiao, X.; Wang, Y. A two-dimensional Ti<sub>3</sub>C<sub>2</sub>T<sub>x</sub> MXene@TiO<sub>2</sub>/MoS<sub>2</sub> heterostructure with excellent selectivity for the room temperature detection of ammonia. *J. Mater. Chem. A* **2022**, *10*, 5505–5519. [[CrossRef](#)]
118. Zhang, S.; Song, P.; Zheng, Y.; Ding, Y.; Wang, Q. MoO<sub>2</sub>/MoO<sub>3</sub>/MXene ternary nanocomposites for high-performance ethanol detection at room temperature. *J. Alloys Compd.* **2022**, *925*, 166663. [[CrossRef](#)]
119. Seekaew, Y.; Kamlue, S.; Wongchoosuk, C. Room-Temperature Ammonia Gas Sensor Based on Ti<sub>3</sub>C<sub>2</sub>T<sub>x</sub> MXene/Graphene Oxide/CuO/ZnO Nanocomposite. *ACS Appl. Nano Mater.* **2023**, *6*, 9008–9020. [[CrossRef](#)]
120. Liu, M.; Song, P.; Liang, D.; Ding, Y.; Wang, Q. 3D porous Ti<sub>3</sub>C<sub>2</sub>T<sub>x</sub> MXene/rGO/SnO<sub>2</sub> aerogel for formaldehyde detection at room temperature. *J. Alloys Compd.* **2022**, *925*, 166664. [[CrossRef](#)]
121. Han, D.; Liu, Z.; Liu, L.; Li, D.; Chen, Y.; Wang, H.; Zhao, L.; Wang, W.; Sang, S. Room temperature and anti-humidity NH<sub>3</sub> detection based on GaN nanorods/Ti<sub>3</sub>C<sub>2</sub>T<sub>x</sub> MXene composite gas sensor. *Sens. Actuators B Chem.* **2023**, *393*, 134319. [[CrossRef](#)]
122. Kuang, D.; Guo, X.; Zhu, Z.; Ding, Y.; Sun, X.; Wu, Z.; Zhang, L.; Zhou, Y.; He, Y. Enhanced room temperature ammonia response of 2D-Ti<sub>3</sub>C<sub>2</sub>T<sub>x</sub> MXene decorated with Ni(OH)<sub>2</sub> nanoparticles. *Ceram. Int.* **2021**, *47*, 19471–19480. [[CrossRef](#)]
123. Fan, J.; Gao, J.; Lv, H.; Jiang, L.; Qin, F.; Fan, Y.; Sun, B.; Wang, J.; Ikram, M.; Shi, K. Synthesis and characterization of an ultra-thin BiOCl/MXene heterostructure for the detection of NO<sub>2</sub> at room temperature with enhanced moisture resistance. *J. Mater. Chem. A* **2022**, *10*, 25714–25724. [[CrossRef](#)]
124. Wu, Q.; Feng, Z.; Wang, Z.; Peng, Z.; Zhang, L.; Li, Y. Visual chemiresistive dual-mode sensing platform based on SnS<sub>2</sub>/Ti<sub>3</sub>C<sub>2</sub> MXene Schottky junction for acetone detection at room temperature. *Talanta* **2023**, *253*, 124063. [[CrossRef](#)]
125. Govardhan, K.; Grace, A.N. Metal/metal oxide doped semiconductor based metal oxide gas sensors—A review. *Sens. Lett.* **2016**, *14*, 741–750. [[CrossRef](#)]
126. Wang, R.; Li, M.; Sun, K.; Zhang, Y.; Li, J.; Bao, W. Element-Doped Mxenes: Mechanism, Synthesis, and Applications. *Small* **2022**, *18*, 2201740. [[CrossRef](#)]
127. Shuvo, S.N.; Ulloa Gomez, A.M.; Mishra, A.; Chen, W.Y.; Dongare, A.M.; Stanciu, L.A. Sulfur-doped titanium carbide MXenes for room-temperature gas sensing. *ACS Sens.* **2020**, *5*, 2915–2924. [[CrossRef](#)]
128. Qiu, J.; Xia, X.; Hu, Z.; Zhou, S.; Wang, Y.; Wang, Y.; Zhang, R.; Li, J.; Zhou, Y. Molecular ammonia sensing of PEDOT: PSS/nitrogen doped MXene Ti<sub>3</sub>C<sub>2</sub>T<sub>x</sub> composite film at room temperature. *Nanotechnology* **2021**, *33*, 065501. [[CrossRef](#)]
129. Liu, M.; Sun, R.Y.; Ding, Y.L.; Wang, Q.; Song, P. Au/ $\alpha$ -Fe<sub>2</sub>O<sub>3</sub>/Ti<sub>3</sub>C<sub>2</sub>T<sub>x</sub> MXene Nanosheet Heterojunctions for High-Performance NH<sub>3</sub> Gas Detection at Room Temperature. *ACS Appl. Nano Mater.* **2023**, *6*, 11856–11867. [[CrossRef](#)]
130. Liu, M.; Sun, R.; Sima, Z.; Song, P.; Ding, Y.; Wang, Q. Au-decorated In<sub>2</sub>O<sub>3</sub> nanospheres/exfoliated Ti<sub>3</sub>C<sub>2</sub>T<sub>x</sub> MXene nanosheets for highly sensitive formaldehyde gas sensing at room temperature. *Appl. Surf. Sci.* **2022**, *605*, 154839. [[CrossRef](#)]

**Disclaimer/Publisher’s Note:** The statements, opinions and data contained in all publications are solely those of the individual author(s) and contributor(s) and not of MDPI and/or the editor(s). MDPI and/or the editor(s) disclaim responsibility for any injury to people or property resulting from any ideas, methods, instructions or products referred to in the content.